Preliminary control and stability analysis of a long-range eVTOL aircraft

Schoser, J.J.; Cuadrat-Grzybowski, M.; Castro, Saullo G.P.

DOI
10.2514/6.2022-1029

Publication date
2022

Document Version
Final published version

Published in
AIAA SCITECH 2022 Forum

AIAA SciTech Forum
January 3-7, 2022, San Diego, CA & Virtual
AIAA SCITECH 2022 Forum

10.2514/6.2022-1029

Preliminary control and stability analysis of a long-range eVTOL aircraft

Jakob J. Schoser* †, Miguel Cuadrat-Grzybowski* ‡, and Saullo G. P. Castro §
Faculty of Aerospace Engineering, Delft University of Technology, 2629 HS Delft, Netherlands

This study proposes a strategy to incorporate control and stability aspects into the preliminary design of a tandem-wing, long-range eVTOL aircraft concept. Four operational phases are considered: cruise, transition, hover, and ground operation. For cruise, a method to design for open-loop stability and size aerodynamic control surfaces is presented. Furthermore, a controller is designed to improve handling qualities. For hover controllability by differential thrust is considered, and for ground operation, the positioning of the landing gear is performed according to clearance and tip-over requirements. A novel analytical model is derived for the tandem wing aircraft in order to estimate during the preliminary design phase the stability derivatives of the aerodynamic forces and moments. The transition manoeuvre between vertical and horizontal flight is only treated with qualitative considerations, due to the highly nonlinear dynamics involved during this flight phase.

I. Introduction

Control and stability of eVTOL vehicles is a challenging topic due to the great variety of flight conditions encountered between vertical take-off and landing, transition and cruise. This study presents a set of methods to be used in the preliminary design stage of an eVTOL aircarft to design for stability and controllability.

The subject of this study is the Wigeon, an eVTOL concept that was developed by ten students at the Delft University of Technology [1]. It is a long-range tandem tilt-wing eVTOL for four passengers designed to take off and land on conventional helipads. The Wigeon is targeted towards European, North American and Southeast Asian markets for comfortable inter-city travel with short door-to-door travel times [2]. The thrust for both vertical and horizontal flight is generated using open propellers [3] placed on the leading edges of the wings, which rotate during the transition phase. A render of the eVTOL can be seen in Figure 1. The most important characteristics of the aircraft are summarised in Table 1. These parameters were obtained through an iterative design process, which incorporated the methods presented in this study [1].

The article begins with a section II on estimating the location of the centre of gravity, which is relevant for stability and control in all flight phases. The subsequent sections are structured according to the different operational phases of the Wigeon. In section III, a novel procedure to evaluate and design for open-loop stability and controllability of tandem-wing aircraft in cruise is presented, along with sizing of aerodynamic control surfaces and the design of a feedback controller to improve handling qualities. Following this, section IV contains an analysis of controllability in hover, and the implications for the centre of mass and rotor placement. In section V, the intermediate stage between cruise and hover is discussed: transition. In section VI, it is explained how considerations of ground stability enter the design process. Section VII, finally, combines the aspects of the previous sections by suggesting a way to integrate stability and control into an iterative, multi-disciplinary design process. The article concludes with an overview of verification procedures in Appendix A, as well as the most important results and recommendations for future work in section VIII.

*These authors contributed equally to this work.
†Corresponding author, MSc student, ORCID: 0000-0002-5663-4921, email: jakob.schoser@gmail.com
‡Corresponding author, MSc student, email: M.Cuadrat-Grzybowski@student.tudelft.nl
§Corresponding author, Assistant Professor, ORCID: 0000-0001-9711-0991, email: S.G.P.Castro@tudelft.nl

Fig. 1 Render of the long-range eVTOL in cruise configuration.

Table 1 Design parameters of Wigeon

Parameter	Value	Parameter	Value
MTOM [kg]	2790.1	Wing span [m]	8.2
OEM [kg]	1428.9	Total wing area [m^2]	19.8
Range [km]	400	Fuselage length [m]	7.3
Cruise speed [m/s]	72.2	Lift to drag ratio [-]	16.3
Stall speed [m/s]	40	No. of engines [-]	12
No. passengers and pilot [-]	5	Maximum thrust per rotor [N]	3745

II. Centre of gravity location

As a first step in each design iteration for stability and control, the centre of gravity (CG) range needs to be identified. The location of the CG depends on the positioning of the aircraft components (which make up the operational empty weight), as well as the loading state. Figure 2 shows an exemplary loading diagram, which illustrates the movement of the CG location during the loading and boarding of the aircraft. The eVTOL must be stable and controllable on the ground and in the air for any CG within this range, such that it can be flown with different loading configurations. With only 7 cm, the CG range is very small. This is due to the passengers, which make up the largest portion of the payload, being located close to the CG. Furthermore, the use of batteries means that neither the mass nor the CG location change during refuelling.

III. Stability and control in cruise

Most of the flight time of the Wigeon will be spent in cruise, so it is essential that the aircraft is easy and safe to fly in this configuration. This section explores stability and control for a tandem wing aircraft with the following structure: subsection III.A derives expressions for the CG limits due to static longitudinal stability and pitch controllability. These limits are then used to perform an optimal sizing and positioning of the wings with respect to each other, as explained in subsection III.B. In subsection III.C, the sizing process for the vertical tail and aerodynamic control surfaces is detailed. This is followed by a derivation of analytical expressions for linearised stability and control derivatives in subsection III.D, as well as simulation results for open-loop dynamics in subsection III.E. Finally, in subsection III.F, a design for a controller is proposed to improve the handling qualities of the Wigeon.

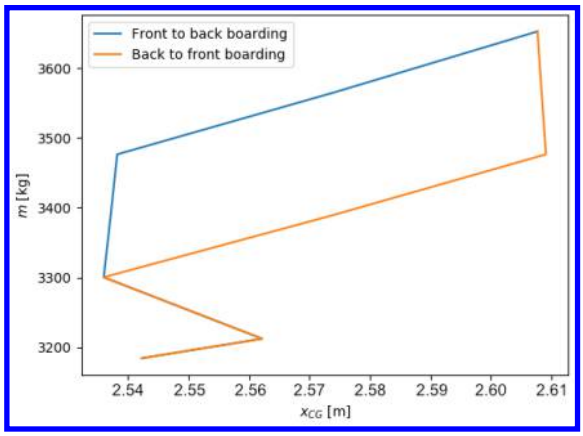

Fig. 2 An exemplary loading diagram, showing the change of the CG x-position as a function of the loading state (origin at the nose, x-axis pointing aft). The assumed order of loading in this case is first luggage, then the pilot, and finally the passengers. Two alternative boarding patterns are shown: back to front and front to back.

A. CG limits due to static longitudinal stability and pitch controllability

All control moments depend on the location of the centre of gravity, since that determines the moment arm that the control force has. However, the pitch moment *M* is especially affected because the weight acts in the X-Z-plane. Therefore, only the criterion for pitch controllability is be addressed here while roll and yaw criteria are discussed in subsection III.C, where the control surfaces are sized.

The free-body diagram of the tandem wing configuration representing straight, symmetric horizontal flight including aerodynamic forces and the weight can be seen in Figure 3.

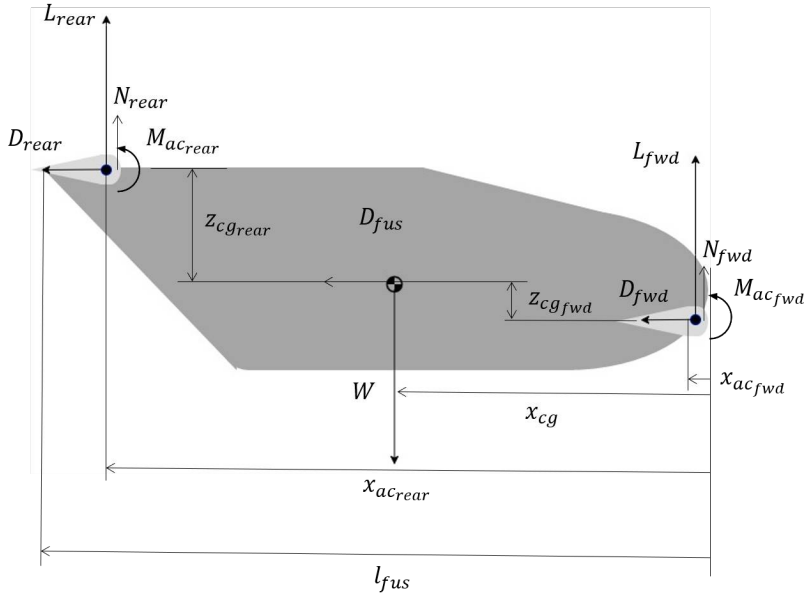

Fig. 3 Free-body diagram showing all aerodynamic loads at horizontal flight with associated distances for the tandem wing configuration.

The non-dimensional moment at the CG is as follows:

$$C_m = C_{m_{ac_{fwd}}} \cdot \frac{S_{fwd}\bar{c}_{fwd}}{S\bar{c}} - C_{D_{fwd}} \cdot \frac{z_{cg_{fwd}}S_{fwd}}{S\bar{c}} + C_{T_{fwd}}\frac{z_{cg_{fwd}}S_{fwd}}{S\bar{c}} + C_{L_{fwd}} \cdot \frac{(x_{cg} - x_{ac_{fwd}})S_{fwd}}{S\bar{c}}$$
$$+ \left(\frac{V_r}{V}\right)^2 \cdot (C_{D_{rear}} \cdot \frac{z_{cg_{rear}}S_{rear}}{S\bar{c}} - C_{L_{rear}} \cdot \frac{(x_{ac_{rear}} - x_{cg})S_{rear}}{S\bar{c}} + C_{m_{ac_{rear}}}\frac{S_{rear}\bar{c}_{rear}}{S\bar{c}} - C_{T_{rear}}\frac{z_{cg_{rear}}S_{rear}}{S\bar{c}}) \quad (1)$$

The subscript fwd is for the forward wing and $rear$ is related to the most aft wing. C_{T_i} is the thrust coefficient defined as the thrust normalised by the dynamic pressure force. V_r is the velocity felt by the rear wing. S and $\bar{c}$ are the mean aerodynamic chord and area of the entire aircraft. In this section the following are assumed to be as:

$$S = S_{fwd} + S_{rear} \quad (2) \qquad \bar{c} = s_{fwd} \cdot \bar{c}_{fwd} + s_{rear} \cdot \bar{c}_{rear} \quad (3)$$

with s_i being the ratio of the wing area S_i by the total area S. $C_{m_{ac}}$ is the aerodynamic moment coefficient at the aerodynamic centre, x_{ac} is the horizontal location of the aerodynamic centre and $z_{cg_{rear}}$ and $z_{cg_{fwd}}$ are the vertical distances between the aerodynamic centre of the rear wing and forward wing respectively and the centre of gravity. It can be seen that the normal force components are neglected as they are known to be small and can be neglected when the free stream is normal to the propeller area [4].

In order to evaluate the aircraft's natural controllability without differential thrust or thrust vectoring, thrust is neglected for further estimations. The further the centre of gravity moves forward, the more difficult it becomes to pitch the aircraft up. In order for it to be controllable, the aircraft must be able to attain $C_m > 0$ even at its most forward centre of gravity position.

$$x_{cg} > \frac{1}{C_{L_{fwd}} + C_{L_{rear}}\frac{S_{rear}}{S_{fwd}}\left(\frac{V_r}{V}\right)^2}\left\{C_{L_{fwd}}x_{ac_{fwd}} + C_{D_{fwd}}z_{cg_{fwd}} - C_{m_{ac_{fwd}}}\bar{c}_{fwd}\right.$$
$$\left. - \left(\frac{V_r}{V}\right)^2\frac{S_{rear}}{S_{fwd}}\left(-C_{L_{rear}}x_{ac_{rear}} - C_{m_{ac_{rear}}}\bar{c}_{rear} + C_{D_{rear}}z_{cg_{rear}}\right)\right\} \quad (4)$$

where the limit of controllability is the trim condition where $C_m = 0$; $C_{L_{fwd}}$ can be influenced by installing mobile surfaces on the trailing edge of the front wing. The distributed rotors would increase their effectiveness and help to achieve higher magnitudes of C_L. These mobiles surfaces are elevators (with elevator deflection δ_e) which increase the control authority over the aircraft.

The limiting factor for static open-loop stability is at high velocities. Hence, the aircraft must be statically stable at cruise where the highest velocity is achieved.

In order to estimate the stability properties of the design, for a step disturbance in the angle of attack α, the moment equation seen in Equation 1 is differentiated w.r.t. to α leading to:

$$C_{m_\alpha} = \partial C_m/\partial\alpha = -C_{D_{\alpha_{fwd}}} \cdot \frac{z_{cg_{fwd}}S_{fwd}}{S\bar{c}} + C_{L_{\alpha_{fwd}}} \cdot \frac{(x_{cg} - x_{ac_{fwd}})S_{fwd}}{S\bar{c}}$$
$$+ C_{D_{\alpha_{rear}}} \cdot (1 - \frac{\partial\epsilon}{\partial\alpha}) \cdot \frac{z_{cg_{rear}}S_{rear}}{S\bar{c}}\left(\frac{V_r}{V}\right)^2 - C_{L_{\alpha_{rear}}} \cdot (1 - \frac{\partial\epsilon}{\partial\alpha}) \cdot \frac{(x_{ac_{rear}} - x_{cg})S_{rear}}{S\bar{c}}\left(\frac{V_r}{V}\right)^2 \quad (5)$$

where $\frac{\partial\epsilon}{\partial\alpha}$ is the downwash effect felt by the rear wing. The latter can be estimated using Equation 6 from [5] (with the addition of η_ϵ).

$$\frac{d\epsilon}{d\alpha} = \eta_\epsilon\frac{K_{\epsilon_\Lambda}}{K_{\epsilon_{\Lambda=0}}}\frac{C_{L_{\alpha_{fwd}}}}{\pi AR_{fwd}}\left\{\frac{r}{r^2 + m_{tv}^2}\frac{0.4876}{\sqrt{r^2 + 0.6319 + m_{tv}^2}} + \left[1 + \left(\frac{r^2}{r^2 + 0.7915 + 5.0734m_{tv}^2}\right)^{0.3113}\right] \cdot \right.$$
$$\left.\left[1 - \sqrt{\frac{m_{tv}^2}{1 + m_{tv}^2}}\right]\right\} \quad (6)$$

where $m_{tv} = 2 \cdot v_t/b$ (where v_t is the vertical distance between the rear wing aerodynamic centre and the forward wing aerodynamic centre). An assumption is made based on the geometry of the aircraft that both wings are perfectly straight,

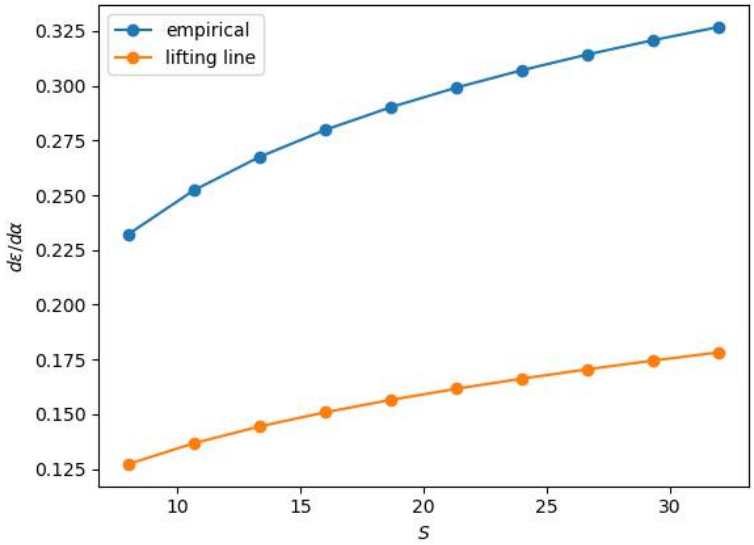

Fig. 4 Variation of the downwash gradient of the front wing on the rear wing with changing total wing surface area (where the ratio of wing areas is kept constant). Both results obtained using Equation 6 and lifting-line theory are displayed.

resulting in v_t being equal to the maximum height of the fuselage. The parameter $r = 2 \cdot (x_{ac_{rear}} - x_{ac_{fwd}})/b_{fwd}$ (with b_{fwd} being the span of the forward wing) and K_{ϵ_Λ} is a function of the quarter chord sweep angle $\Lambda_{c/4}$ of the forward wing [6].

The factor η_ϵ is a correction factor applied to the downwash gradient to better match the results obtained using the lifting line theory [7]. Figure 4 shows an exemplary sensitivity analysis of the downwash gradient, which reveals that Equation 6 overestimated the downwash gradient by roughly a factor of 2. Therefore, it is set that $\eta_\epsilon = 0.5$.

Furthermore, for propeller aircraft, an additional downwash is created due to the propellers which has to be taken into account. This is written as follows [6]:

$$\left(\frac{d\epsilon}{d\alpha}\right)_p = 6.5(sin(6\phi))^{2.5} \cdot \left(\frac{\rho \cdot P_{br}^2 \cdot S_{fwd}^3 \cdot C_{L_{fwd}}^3}{l_h^4 \cdot W^3}\right)^{1/4} \tag{7}$$

where ϕ is the angle between the wings defined as $\phi = arcsin(m_{tv}/r)$, P_{br} is the shaft power per engine and $C_{L_{fwd}}$ is the lift coefficient for the cruise condition.

It is now essential to estimate the drag derivatives C_{D_α} using the polar drag equation leading to:

$$C_{D_{\alpha_i}} = 2 \cdot C_{L_{\alpha_i}} \frac{C_{L_i}}{\pi A R_i e_i} \tag{8}$$

with C_{L_i} being the lift coefficient of one of the wings in cruise condition.

For static longitudinal stability, it is required that $C_{m_\alpha} < 0$, such that the aircraft restores its initial state after a disturbance in angle of attack. This results in the neutral stability CG position curve as follows:

$$x_{cg} = \left(\frac{C_{L_{\alpha_{fwd}}} x_{ac_{fwd}} + C_{D_{\alpha_{fwd}}} z_{cg_{fwd}} + (C_{L_{\alpha_{rear}}} \frac{x_{ac_{rear}} S_{rear}}{S_{fwd}} - C_{D_{\alpha_{rear}}} z_{cg_{rear}})(1 - \frac{\partial\epsilon}{\partial\alpha}) \left(\frac{V_r}{V}\right)^2}{C_{L_{\alpha_{fwd}}} + C_{L_{\alpha_{rear}}} \frac{S_{rear}}{S_{fwd}} (1 - \frac{\partial\epsilon}{\partial\alpha}) \left(\frac{V_r}{V}\right)^2}\right) \tag{9}$$

At this point, it is essential to verify the sensitivity of the latter equation w.r.t to the aspect ratio design variable. As it can be seen that $x_{cg_{max}}$ is a function of C_{L_α} of both wings and that the latter is a function of the aspect ratio AR, it must be seen how sensitive the maximum value is to a change in the aspect ratio. This is illustrated in Figure 5.

From Figure 5, it can be seen that the most aft allowable cg position does vary significantly. An increase in aspect ratio is hence favourable for the stability limit. This must be taken into consideration for future design phases.

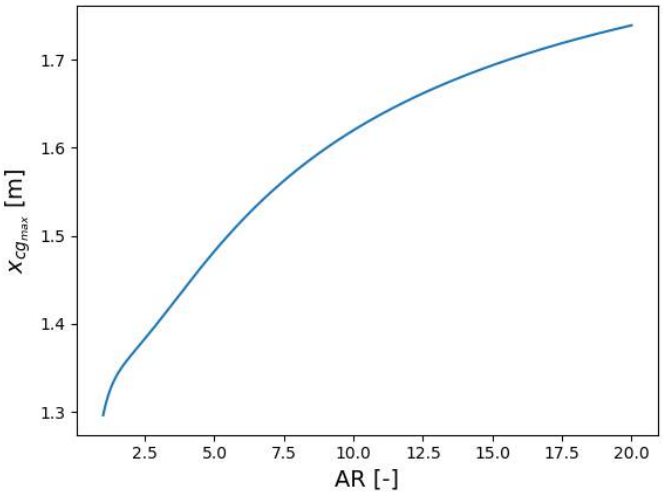

Fig. 5 Sensitivity analysis on the aft CG position as a function of AR.

B. Relative wing sizing and placement

As Equation 9 shows, the location of the neutral point and thus static longitudinal stability in cruise depends strongly on the geometry and positioning of the wings. More specifically, it depends on the ratio of wing surfaces S_{rear}/S_{fwd}, $x_{ac_{fwd}}$, $x_{ac_{rear}}$, $z_{cg_{fwd}}$, and $z_{cg_{rear}}$. Moreover, there are indirect geometric dependencies through other terms in Equation 9.

$C_{L_{\alpha_{fwd}}}$ and $C_{L_{\alpha_{rear}}}$ do not only depend on the C_{l_α} of their respective aerofoils. Instead, they are given by Equation 10 [8]. From this, it can be seen that C_{L_α} depends on wing aspect ratio, sweep and aerofoil lift slope. The last two are taken as fixed based on aerodynamic considerations [7]. Therefore, the aspect ratio AR remains as a free design variable.

$$\frac{dC_L}{d\alpha} = C_{L_\alpha} = \frac{C_{l_\alpha}\, AR}{2 + \sqrt{4 + \left(\frac{AR\,\beta}{\eta}\right)\left(1 + \frac{\tan(\Lambda_{0.5C})^2}{\beta^2}\right)}} \tag{10}$$

Another implicit geometric dependency of the neutral point location stems from the downwash gradient $\frac{\partial \epsilon}{\partial \alpha}$. As shown in Equation 6 and Equation 7, this parameter depends on the aspect ratio AR_{fwd}, span b_{fwd} and surface area S_{fwd} of the forward wing, and the horizontal and vertical distance between the wings (Δx and Δz, respectively). Note that Equation 9 neglects the impact of the upwash of the rear wing on the front wing. This is deemed an acceptable simplification as an analysis using lifting line theory showed that the upwash gradient to be an order of magnitude lower than the downwash gradient [7].

In addition to this, there are dependencies on the vertical wing positions, aspect ratios and cruise lift coefficients through the drag contributions. Finally, the term $(V_r/V)^2$ is taken as 1, which is the value suggested by [5] for a high-mounted stabiliser. This value was chosen since the vertical distance between the wings is similar as between a low-mounted wing and a high-mounted stabiliser, while the horizontal distance is even greater.

As for the forward CG limit for pitch controllability, similar geometric dependencies could be identified. Again, S_{rear}/S_{fwd}, $x_{ac_{fwd}}$, $x_{ac_{rear}}$, $z_{cg_{fwd}}$, and $z_{cg_{rear}}$ are directly included in the equation (Equation 4). However, the only influence of the aspect ratio is on the drag coefficients of the wing, which is a small effect that makes controllability less dependent on aspect ratio. In addition to these, the length of the mean aerodynamic chords $\bar{c}_{fwd}$ and $\bar{c}_{rear}$, as well as the maximum increase in $C_{L_{fwd}}$ that the elevators can offer. This is discussed in more depth in subsection III.C.

A sensitivity study of the neutral point and controllability limit found that S_{rear}/S_{fwd} and AR_{fwd} are the most powerful parameters to affect the stability and controllability limits of the aircraft (see [1, 2, 9]). The relative wing size strongly affects both stability and controllability, while the front wing aspect ratio mainly impacts stability. A_f is especially important since it not only impacts the lift slope of the front wing, but also the downwash which in turn impacts the rear wing.

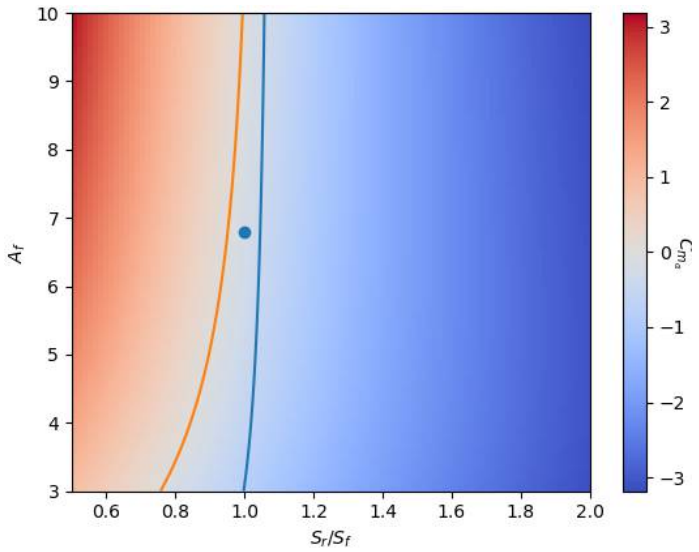

Fig. 6 Heat map showing C_{m_α} as a function of the front wing aspect ratio and the ratio between wing surface areas. The orange line indicates the limit for static longitudinal stability, while the blue line indicates the limit for pitch controllability at stall. The blue line denotes the design point of the Wigeon.

Having identified these two key design variables allowed to plot the constraints affecting wing placement and sizing as contour lines in a 2D plot with S_{rear}/S_{fwd} on one axis and AR_{fwd} on the other. Such a plot can be seen in Figure 6. Note that the total wing area is kept constant as to not affect the lift of the aircraft in cruise.

The plot shows that a small aspect ratio on the front wing is required for longitudinal stability, implying an increase in induced drag. Also, since the root chord is limited in order to not interfere with other elements of the aircraft, the small aspect ratio would require a short wingspan.

The consequent reduction in the space available for rotors on the front wing could mean that rotors would have to be relocated from the front wing to the back wing, meaning that the front rotors would have to perform at a higher throttle setting in hover than the rear engines. Reducing the number of engines on the front wing could also have a negative impact on control redundancy in hover. The outcome of this analysis agrees with the results from [10], who found that reducing the aspect ratio of the front wing in a tandem-wing eVTOL aircraft to 25% of the rear wing could allow it to be longitudinally stable.

C. Vertical tail and control surface design

In horizontal flight, there are nine state variables to be controlled [11]. As in conventional aircraft, the Wigeon controls these states using the control surfaces that create rolling, pitching, and yawing moments.

The choice of aerodynamic control surfaces, as opposed to differential thrust and thrust vectoring, is based on the findings of Chen [12], who concluded that conventional aerodynamic surfaces are much more effective for steady level flight than thrust vectoring.

In addition to this, a vertical tail is designed since it was found that a tandem wing is generally unstable in the lateral direction (see [1]).

1. Vertical tail and rudder sizing

This section presents the different required steps to size of the vertical tail, in terms of its required surface area, starting from an initial estimate obtained using a class I method. After sizing the vertical tail, the stability requirements and finally controllability requirements are derived for a one engine inoperative (OEI) condition. The highest value obtained from either the stability or controllability requirement is chosen as the final design.

In order to initialise the analysis and sizing, a so-called class I method [13] is used. This method assumes a vertical tail volume coefficient $\bar{V}_v$ which yields an equation for the tail area S_v being as follows:

$$S_v = \bar{V}_v \cdot \frac{Sb}{l_v} \tag{11}$$

where l_v is the vertical tail moment arm as $l_v = (x_v - x_{cg})$. A value of 0.04 for the volume coefficient is chosen (as initial estimate) using values found in [13]. Furthermore, it is assumed that the vertical tail is placed at the end of the fuselage. Due to the assumed small size of the vertical tail w.r.t. to the fuselage length, l_{fus}, this results in initial estimate for the aerodynamic centre of the vertical tail to be $x_v \approx l_{fus}$. Additionally, an estimate of the root chord, c_{v_r}, must be performed from the surface area and taper ratio λ_v. Furthermore, b_v is the vertical tail span which can be obtained from $b_v = \sqrt{AR_v \cdot S_v}$. The initial value for AR_v is assumed to be 1.25, chosen using [13] and later its sensitivity to S_v and b_v is verified in order to understand the importance of this design parameter. The aspect ratio is also treated as a design variable in the multi-disciplinary framework [1]. Furthermore, another design variable is the TE (trailing edge) sweep angle, $\Lambda_{v_{TE}}$ which is also maximised or optimised (in order to increase the effective moment arm l_v and in order to have rudder outside the wake of the rear wing as much as possible). The final design variable is the taper ratio, λ_v, chosen to be initially 0.40 in order to obtain an approximated elliptical side force distribution. With these design variables, it is possible to compute the required aerodynamic and geometric properties starting from the MAC, $\bar{c}_v$, and the root chord, c_{v_r} using:

$$\bar{c}_v = 2/3 \cdot c_{v_r} \cdot \frac{(1 + \lambda_v + \lambda_v^2)}{(1 + \lambda_v)} \tag{12}$$

$$c_{v_r} = \frac{2}{1 + \lambda_v} \cdot \frac{S_v}{b_v} \tag{13}$$

Having the obtained the initial values, a more accurate estimate of the moment arm, l_v, can be done by using the x-and y-positions of the LEMAC of the vertical tail (which are a function of the TE sweep), assuming that the root chord is entirely on the fuselage and finally that the aerodynamic centre is at quarter-chord of the MAC. The moment arm becomes:

$$l_v = l_{fus} - c_{v_r} + X_{LEMAC_v} + 0.25 \cdot \bar{c}_v \tag{14}$$

where X_{LEMAC_v} is the LEMAC position in the x-direction (from the leading edge of the aerodynamic surface), computed as follows:

$$Y_{MAC_v} = \frac{b_v}{6} \cdot \frac{1 + 2 \cdot \lambda_v}{1 + \lambda_v} \tag{15}$$

$$X_{LEMAC_v} = Y_{MAC_v} \cdot tan(\Lambda_{LE_v}) \tag{16}$$

It is now possible to present the two different requirements that the vertical tail must satisfy.

Having initialised the vertical tail design, the stability requirement must be specified. In fact, in order to have lateral static stability it must hold that: $C_{n_\beta} > 0$. This stability derivative has multiple components: the wing terms, the fuselage term and finally the vertical tail component.
First the wing contribution, for unswept wings (at quarter-chord) is derived using [8] and is as follows:

$$(C_{n_\beta})_w = C_L^2 \cdot \frac{1}{4\pi AR_w} \cdot \frac{S_w b_w}{Sb} \tag{17}$$

where the subscript w refers to one wing and C_L is the lift coefficient at cruise. The second required terms for the computation of C_{n_β} is the fuselage term estimated using [14] with Equation 18 and Equation 19:

$$(C_{n_\beta})_{fus} = -\frac{2\nu}{Sb} \tag{18}$$

$$\nu = \int_0^{l_{fus}} \frac{\pi}{4} \cdot w(x)^2 dx \tag{19}$$

where ν is the effective volume of the fuselage and $w(x)$ is the width as a function of the longitudinal position x starting from the nose. This are approximated with an elliptical shape resulting in $w(x) = (w_{max}/2) \cdot \sqrt{1 - \left(\frac{x}{l_{fus}/2}\right)^2}$.

The third term is related to the vertical tail as follows:

$$(C_{n_\beta})_v = -C_{Y_{v_\alpha}} \cdot \left(1 - \frac{d\sigma}{d\beta}\right) \cdot \left(\frac{V_v}{V}\right)^2 \cdot \frac{S_v l_v}{Sb} \tag{20}$$

where $(C_{Y_{v_\alpha}})_v$ is the derivative of the side force coefficient C_Y (of the vertical tail) w.r.t α. This derivative is basically negative C_{L_α} of the vertical tail. σ is the side wash (assumed to be 0 for simplicity) and V_v is the velocity of the airflow at the vertical tail (assumed to be equal to the aircraft airspeed as the flow would be undisturbed due to the height difference between the wings).

The final equation relating to the stability requirement for S_v can be derived and results in Equation 21.

$$S_v = \frac{(C_{n_\beta} - (C_{n_\beta})_{fus} - (C_{n_\beta})_{w,rear+fwd})}{C_{L_{v_\alpha}}} \cdot \frac{Sb}{l_v} \tag{21}$$

where C_{n_β} is taken to be 0.0571 in order to provide a sufficient stability margin as found in [15] and to account for the previously defined assumptions.

For the controllability condition, the vertical tail should provide a sufficient counter-acting yaw moment for an asymmetric thrust condition.

In order to obtain a reasonable estimate, several design variables must be identified being the maximum rudder deflection $\delta_{r_{max}}$, the span and chord ratio of the rudder and the vertical tail $\frac{b_r}{b_v}$ and $\frac{\bar{c}_r}{\bar{c}_v}$ respectively and the minimum controllable speed V_{MC}. These are estimated using [16] and can be summarised in Table 2.

Table 2 Lateral design variables.

Design variable	Value/Range
$\delta_{r_{max}}$ [deg]	25
b_r/b_v [-]	0.7-1.0
$\bar{c}_r/\bar{c}_v$ [-]	0.15-0.4
V_{MC}/V_{stall} [-]	1.2

For the geometric parameters such as $\frac{b_r}{b_v}$ and $\frac{\bar{c}_r}{\bar{c}_v}$, a sensitivity analysis towards S_v is performed in order to verify the most optimal pair of values for the lowest area.

Additionally, the same is performed for a combination of $\Lambda_{v_{TE}}$ and AR_v.

For the controllability requirement, the vertical tail and rudder must be sized in such a manner that an OEI condition can be controlled, where the OEI is defined in this section as losing all engines from one side of the aircraft. The created yaw moment due to an asymmetric thrust condition can be computed using Equation 22 to Equation 24 [15]:

$$N_a = N_E + N_D \tag{22}$$

$$N_E = 2\sum_i^n \frac{T}{n_E} y_i \tag{23}$$

$$N_D \approx 0.25 \cdot N_E \tag{24}$$

where N_E is the sum of the individual asymmetric yaw moments due to an asymmetric thrust per engine T/n_E, with a moment arm y_i and finally n being the number of engines on one half-wing. N_D is the yaw moment due to the drag of the engine (which for variable pitch propellers is a quarter of N_E [15]) and n_E is the number of propellers.

It is now possible to show the yaw moment equilibrium equation which relates to the lateral trim condition obtained with Equation 25 and Equation 26 [16]:

$$N = N_0 + N_a + N_{\delta_r} \cdot \delta_r + N_\beta \cdot \beta + N_{\delta_a} \cdot \delta_a = 0 \tag{25}$$

$$C_{n_{\delta_r}} = -C_{L_{v_\alpha}} \cdot \frac{S_v l_v}{Sb} \cdot \tau_r \cdot \frac{b_r}{b_v} \tag{26}$$

with $N_0 = 0$ as the vertical tail has a symmetric airfoil, $C_{n_{\delta_r}}$ is the yaw control derivative w.r.t rudder deflection and τ_r being the rudder effectiveness which is as follows [16]:

$$\tau_r = 1.129 \cdot \left(\frac{\bar{c}_r}{\bar{c}_v}\right)^{0.4044} - 0.1772 \tag{27}$$

Assuming that the aircraft is not slipping ($\beta = 0$) and no aileron deflection is applied ($\delta_a = 0$), an equation for S_v can be obtained. The aforementioned is as follows:

$$S_v = \frac{N_a}{0.5\rho V_{MC}^2 \cdot C_{L_{v_\alpha}} \cdot l_v \cdot \tau_r \cdot (b_r/b_v) \cdot \delta_r} \tag{28}$$

Having derived the stability and controllability limits for S_v with Equation 21 and Equation 28, the limiting case must be identified and as a result the highest value obtained from both equations is used for the final design.

It is now possible to find the sensitivity of the surface area S_v and the span b_v for the set of design variables and in the same time find an optimal value. First, the $\Lambda_{v_{TE}}$ with AR_v pair is selected as can be seen in Figure 7.

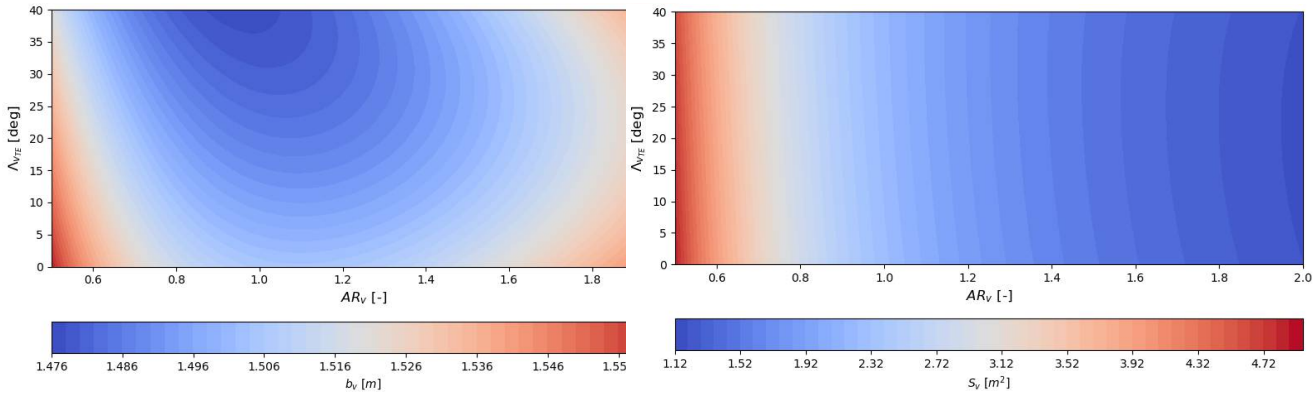

(a) Sensitivity of the vertical tail span, b_v as a function of $\Lambda_{v_{TE}}$ with AR_v.

(b) Sensitivity of the vertical tail span, S_v as a function of $\Lambda_{v_{TE}}$ with AR_v.

Fig. 7 Sensitivity analysis of both b_v and S_v parameters.

It can be easily seen, that S_v has a very low sensitivity to the sweep angle, whereas it decreases with increases AR_v. The span, b_v, on the other hand has a localised minimum around ($AR_v = 1.05, \Lambda_{v_{TE}} = 39\,\text{deg}$). It is therefore necessary to find a compromise between both the surface area and the span, and it must be noted that the larger the span and sweep, the larger the required structure to support it, which increases the mass. It is hence decided that an AR_v of 1.4 and a TE sweep of 25 deg is a good choice when taking into account all the aforementioned. Finally, it is possible to select the required $\frac{b_r}{b_v}$ and $\frac{\bar{c}_r}{\bar{c}_v}$ in order to match the both the controllability and stability (represented as a black contour line) requirements and can be seen in Figure 8.

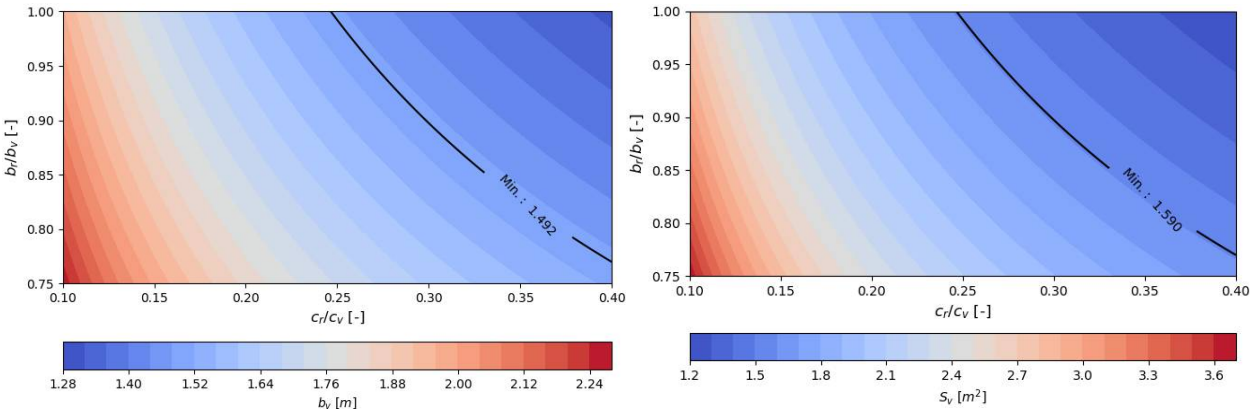

(a) Sensitivity of the vertical tail span, b_v as a function of $c\frac{b_r}{b_v}$ and $\frac{\bar{c}_r}{\bar{c}_v}$, for the selected aspect ratio and sweep.

(b) Sensitivity of the vertical tail area, S_v as a function of $\frac{b_r}{b_v}$ and $\frac{\bar{c}_r}{\bar{c}_v}$, for the selected aspect ratio and sweep.

Fig. 8 Sensitivity analysis of both S_v and b_v for the controllability design variables and the stability requirement.

From Figure 8, it can clearly be seen that both variables are sensitive and affected in the same manner by the design variables. Therefore, to provide the most optimum values in terms of stability and to provide less stress to the vertical tail, the values are taken to be: $\frac{b_r}{b_v} = 1.0$ and $\frac{\bar{c}_r}{\bar{c}_v} = 0.24$.

Finally, following the S_v estimation it is possible to estimate all geometric properties of the vertical tail and rudder. These can be visualised in Figure 9 for the specific example.

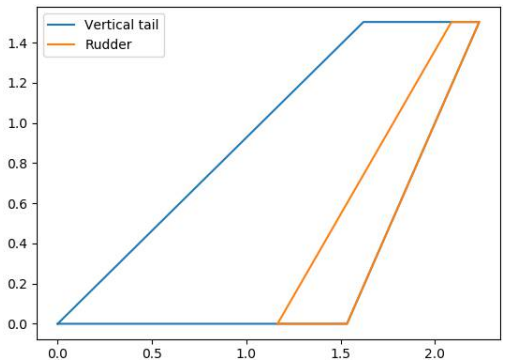

Fig. 9 Visualisation of the vertical tail and rudder with geometrical properties $b_v = 1.503$ m, root chord $c_{v_r} = 1.534$ m and tip chord $c_{v_t} = 0.613$ m.

2. Elevator sizing

The elevator is an essential control surface for pitch control authority, especially it is vital at low speeds as it is the limit of controllability. As it is done for previous control surfaces, it is required to assume a range for a set of design variables in order to obtain the best elevator sizing possible (that can be found in [17]). The choice of designing a simple elevator or an elevon is to be verified by checking what are the required geometric properties for pitch control at the lowest speed and what would the value of the specific span dimensions have to be computed. For the specific case study, upon further scrutiny of both the aileron and elevator sizing, the pitching control surface is defined to be an elevon placed on both the forward and rear wings, working in a similar manner to an aileron but for pitch control. This is because it was found that high span ratio values are needed for the control surfaces.

It is noted that a certain increase in $C_{L_{fwd}}$ and a decrease in $C_{L_{rear}}$ are needed in order to obtain a feasible CG range (see [9]). This ensures not only that the aircraft can be trimmed at stall, but also that the elevators can be utilised to control the aircraft in all other horizontal flight conditions. The general lift coefficient equation can be seen in Equation 29. The previously described required increase in lift coefficient, caused by the elevator deflection, can be identified and re-written in Equation 30.

$$C_{L_i} = C_{L_{\alpha_i}} \cdot \alpha + C_{L_{\delta e_i}} \cdot \delta_e \tag{29}$$

$$\Delta C_{L_i} = \pm C_{L_{\delta e_i}} \cdot \delta_e \tag{30}$$

where $C_{L_{\delta e_i}}$ is the control derivative of one of the lift coefficients w.r.t a deflection input. It can be observed that for the rear wing, the required change in lift coefficient is negative whereas for the forward a positive change is required to obtain better pitching up capability.

The control derivative can estimated using Equation 31 [17] with an additional derived correction factor to account for the fuselage width clearance:

$$C_{L_{\delta e_i}} \approx \tau_e \cdot \frac{b_e}{b_i} \cdot C_{L_{\alpha_i}} \tag{31}$$

where τ_e is the elevator effectiveness which can also be computed using Equation 37, where the ratio to be used is S_e/S_i. It must also be noted that the aircraft's control derivative $C_{L_{\delta_e}}$ is different from the above. However, this aircraft derivative is not required as the elevator is designed for a specific increase and decrease in the forward and rear lift coefficient, respectively, and not for the entire aircraft. It can therefore be possible to optimise for the best set of S_e/S_i and b_e/b_i, where a special attention must be placed on the chord ratio as well in order to minimise the impact on the wing box. As a last note, a clearance w_{clear} of 0.5 m is taken in order to account for a local fuselage width of 1 m.

Finally, the elevators must be able to trim and allow for a pitching up moment at stall which can be translated to $C_m > 0$. Using Equation 1, it can be seen that the moment coefficient is a function of both lift coefficients and hence by extension the elevator deflection δ_e and the respective wing control derivatives. In order to affect the flow over the rear wing as little as possible, a maximum elevator deflection of 10deg is chosen (which is smaller than what can be found in [17]). The sensitivity analysis of the pitching moment coefficient w.r.t S_e/S_i, $\bar{c}_e/\bar{c}_i$ and the elevator span ratio b_e/b_i can now be performed and visualised in Figure 10.

A similar pattern is observed for both the area and chord ratio design variables due to their geometric relationship. However, it can be noticed that the moment coefficient is slightly more sensitive to the chord ratio (although it has a

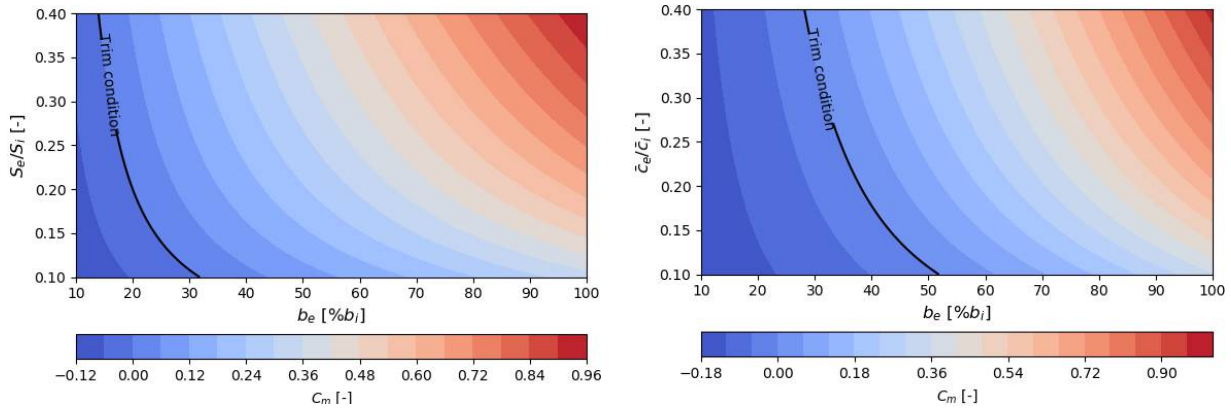

(a) Sensitivity of C_m as a function of area ratio $\frac{S_e}{S_i}$ and b_e in percentages of wing span b_i.

(b) Sensitivity of C_m as a function of $\frac{\bar{c}_e}{\bar{c}_i}$ and b_e in percentages of wing span b_i.

Fig. 10 Sensitivity of the pitching moment coefficient w.r.t. S_e/S_i, $\bar{c}_e/\bar{c}_i$ and b_e for a maximum elevator deflection of $\delta_e = 10\,\text{deg}$.

more restricted design space due to the presence of the wingbox). For the elevon wingspan ratio, a value of $\frac{b_e}{b_i} = 0.868$ is selected due to the fuselage clearance constraint. The outer limit of the elevator is placed at 99% of the wing's span in order to ensure good roll control when designing the ailerons. As previously mentioned, the limiting design variable is the chord ratio which is selected to be $\frac{\bar{c}_e}{\bar{c}_i} = 0.25$. In the same manner as for the rudder, the selected design ratios can be multiplied by the wing geometric properties in order to obtain the elevator size.

3. Aileron sizing

In order to design and size the ailerons, the roll rate requirement for small aircraft is needed. The aircraft must be able to roll faster or at the same rate as demanded by regulations. This involves a combination of the airfoil aerodynamics, wing geometry and finally a control derivative estimation.

As a first step, some design variables must be identified and defined. These are: the aileron-wing surface and span ratio, S_a/S_i and b_a/b respectively and the maximum aileron deflection $\delta_{a_{max}}$. The aileron span is found by assuming the inner and outer positions, b_1 and b_2 respectively, leading to $b_a = b_2 - b_1$ as can be seen in Figure 11. The chosen values and ranges of the geometric parameters are summarised in Table 3 as seen in literature [18].

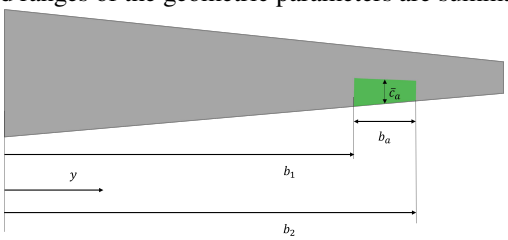

Fig. 11 Aileron geometry, position w.r.t the wing and coordinate y used.

Table 3 Aileron design variables.

Design variable	Value/Range
$\delta_{a_{max}}$ [deg]	± 30
$b_2/(b_i/2)$ [-]	0.70-0.95
S_a/S_i [-]	0.05-0.2

Due to the elevon wingspan and relative position on both wings, $b_2 = 0.99 \cdot b_i/2$. The outer position of the aileron is hence slightly higher than as it can be found in Table 3. A maximum deflection of $\delta_{a_{max}} = \pm 30\,\text{deg}$ is assumed. Furthermore, a particular attention must be noted on the range of S_a/S_i (which can be seen in Table 3), as for conventional aircraft the typical range is 0.05-0.1 [18]. This difference is taking into account the tandem wing nature of the eVTOL, hence S_i can reach values that are less than half the value of the total area S. This hence explains the higher maximum limit set for the surface ratio and the lower limit for the inner limit.

Having defined the necessary geometric properties, the physical problem can be explained. Due to its relatively small mass, the aircraft must be able to roll 60 deg in 1.3 s [19]. This is further confirmed for V/STOL aircraft in [11],

where the requirement is slightly lower. For this the following equilibrium equation for steady roll is used:

$$\mathcal{L} = \mathcal{L}_\beta \cdot \beta + \mathcal{L}_p \cdot \frac{pb}{2V} + \mathcal{L}_{\delta_r} \cdot \delta_r + \mathcal{L}_{\delta_a} \cdot \delta_a = 0 \tag{32}$$

where p is the roll rate and for a pure roll $\beta = 0$ and no deflection in rudder is used $\delta_r = 0$. The latter with the regulation requirement yield the following:

$$p = -\frac{2V}{b} \cdot \frac{C_{l_{\delta_a}}}{C_{l_p}} \cdot \delta_{a_{max}} \geq \pm \frac{60 \cdot \pi/180}{1.3} \tag{33}$$

with V being the slowest speed at which a controlled roll manoeuvre can be performed which is assumed to be V_{MC}.

It is further assumed that the wing is straight, and this assumption is supported by the fact that the sweep at quarter-chord is 0 and due to that the wing is approximately straight. It is now possible to estimate two required derivatives, $C_{l_{\delta_a}} = \frac{dC_l}{d\delta_a}$ and $C_{l_p} = \frac{dC_l}{d\frac{pb}{2V}}$, obtained using simple strip theory[14, 20]. These can be found using Equation 34 [18] and Equation 35 [20].

$$(C_{l_{\delta_a}})_i = -\frac{C_{L_{\alpha_i}} \tau_a c_{r_i}}{S_i b_i} \left[\frac{y^2}{2} + \frac{2}{3} \frac{\lambda_i - 1}{b_i} y^3 \right]_{b_2}^{b_1} \tag{34}$$

$$(C_{l_p})_i = -\frac{(C_{l_{\alpha_i}} + C_{d_{0_i}}) c_{r_i} b_i}{24 \cdot S_i} (1 + 3\lambda_i) \tag{35}$$

where C_{l_α} and C_{d_0} are lift curve slope and zero lift drag coefficient of the wing airfoil and i refers to either the forward or rear wing. It must be noted that in order to obtain the aircraft's $C_{l_{\delta_a}}$ and C_{l_p}, a correction factor which accounts for the different wing sizes has to be implemented. This is due to the definition of the aircraft's roll moment coefficient C_l as:

$$C_l = \frac{\mathcal{L}_{fwd} + \mathcal{L}_{rear}}{0.5\rho V^2 \cdot Sb} = C_{l_{fwd}} \cdot \frac{S_{fwd} b_{fwd}}{Sb} + C_{l_{rear}} \cdot \frac{S_{rear} b_{rear}}{Sb} \left(\frac{V_r}{V} \right)^2 \tag{36}$$

where b is the span of the entire aircraft. Finally, τ_a is the aileron effectiveness that can be estimated using Equation 37 [18].

$$\tau_a = -6.624 \cdot \left(\frac{S_a}{S_i} \right)^4 + 12.07 \cdot \left(\frac{S_a}{S_i} \right)^3 - 8.292 \cdot \left(\frac{S_a}{S_i} \right)^2 + 3.295 \cdot \left(\frac{S_a}{S_i} \right) + 0.004942 \tag{37}$$

With all the aforementioned, it is now possible to proceed with the sizing procedure. This must ensure that Equation 33 is satisfied and with an assumed b_2 value, optimal values for S_a/S_i and b_1 can be obtained through a sensitivity analysis. Additionally, the aileron is constrained within the geometry of the elevon and this is evaluated as follows:

$$\frac{S_a}{S_i}(b_1) = \frac{1}{S_i} \frac{c_{a_t} + c_{a_r}(b_1)}{2} \cdot 2 \cdot b_a(b_1) \tag{38}$$

with c_{a_t} and c_{a_r} being the tip and root chords respectively. All the aforementioned can be visualised with Figure 12.

From Figure 12, it can be seen that both variables affect the roll rate of the aircraft in a similar manner. The intersection of the geometric constraint from Equation 38 and the roll requirement is the most optimum design for the aileron. This is found to be: $\frac{S_a}{S_i} = 0.115$ and $b_1 = 0.4703 \cdot b_{fwd}/2$.

The final elevon design, for the specific example, can be be visualised (for the forward wing) in Figure 13.

D. Stability and control derivatives

In the following, a novel analytical model is derived for the tandem wing aircraft in order to estimate during the preliminary design phase the stability derivatives of the aerodynamic forces and moments X (forward force), Z (down force) and M (pitch moment) for longitudinal motions and Y (side force), $\mathcal{L}$ (roll moment) and N (yaw moment) for lateral motion. The state variables for longitudinal motion are: the dimensionless velocity perturbation $\hat{u}$, the angle of attack α, the pitch angle θ, and the dimensionless pitch rate $\frac{q\bar{c}}{V_0}$. In the case of lateral motion the state variables are: the side-slip angle β, the bank angle ϕ, the dimensionless roll and yaw rates $\frac{pb}{2V_0}$ and $\frac{rb}{2V_0}$ respectively. This method combines both known semi-empirical methods (that are adapted to account for a two-winged aircraft) and new physical derivations. The preliminary model is verified using stability derivatives obtained for other aircraft from [11].

1. Longitudinal aerodynamic forces

The corresponding longitudinal aerodynamic force coefficients C_X and C_Z are as follows:

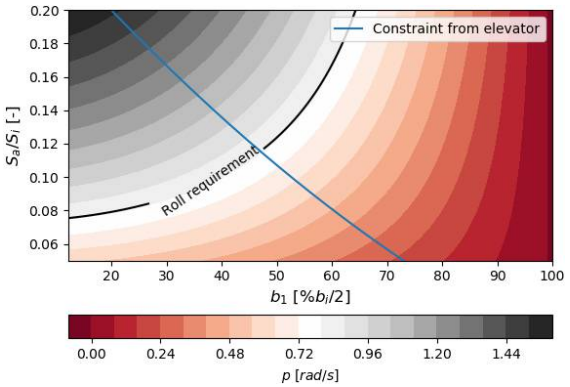

Fig. 12 Sensitivity analysis of the roll rate, p, as a function of the surface ratio S_a/S_i and the inner dimension b_1.

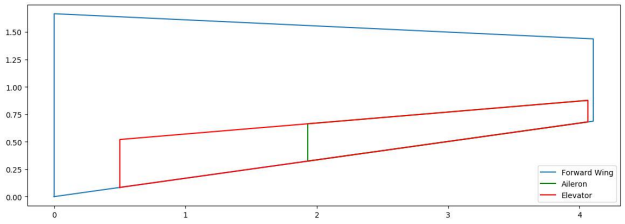

Fig. 13 Elevon geometry visualisation for the forward wing.

$$C_X = C_L sin(\alpha) - C_D cos(\alpha) + C_T \tag{39}$$

$$C_Z = -C_L cos(\alpha) - C_D sin(\alpha) + C_T i_T \tag{40}$$

with α being the angle of attack, C_T being the thrust coefficient defined previously and i_T being the effective incidence angle of the propeller total thrust force w.r.t to the stability axis system.

When estimating the dynamic stability behaviour of the aircraft, the main focus is on small disturbances that deviate the aircraft from its trim (equilibrium) condition. Due to the aforementioned, the small angle approximation can be used for the angle of attack, resulting in:

$$C_X \approx C_L \alpha - C_D + C_T \tag{41}$$

$$C_Z \approx -C_L - C_D \alpha \tag{42}$$

The aerodynamic pitching moment coefficient, C_m, has already been derived and can be found in Equation 1.

2. Velocity stability derivatives

The first stability derivatives to be discussed in this section are the derivatives w.r.t $\hat{u} = \frac{\Delta V}{V_0}$, the change in initial velocity normalised by the initial velocity V_0 (in trim condition). The derivatives are hence C_{X_u}, C_{Z_u} and C_{m_u}. Using Equation 41, Equation 42 and Equation 1 and the transformation $\frac{d}{d\hat{u}} = M\frac{d}{dM}$, the equations are as follows:

$$C_{X_u} = \frac{M_0^2}{1 - M_0^2} C_{L,0}\alpha_0 - 3C_{D,0} - 3C_{L,0} tan(\gamma_0) - M_0 C_{D_M} \tag{43}$$

$$C_{Z_u} = -\frac{M_0^2}{1 - M_0^2} C_{L,0} - M_0 C_{D_M}\alpha_0 \tag{44}$$

$$C_{m_u} = M_0 \cdot \left[C_{L_{M_{fwd}}} \cdot (x_{cg} - x_{ac_{fwd}}) \cdot \frac{S_{fwd}}{S\bar{c}} - C_{L_{M_{rear}}} \cdot (x_{ac_{rear}} - x_{cg}) \cdot \frac{S_{rear}}{S\bar{c}} \left(\frac{V_r}{V}\right)^2 \right] + C_{T_{u_{fwd}}} \frac{z_{cg_{fwd}} S_{fwd}}{S\bar{c}} - C_{T_{u_{rear}}} \frac{z_{cg_{rear}} S_{rear}}{S\bar{c}} \left(\frac{V_r}{V}\right)^2 \tag{45}$$

where the subscript 0 relates to the initial equilibrium condition being the cruise condition, M_0 is the initial mach number, γ_0 is the initial flight path angle and finally $C_{L_{i_M}}$ and C_{D_M} are the lift and drag derivatives w.r.t mach number which account for compressibility effects. The latter drag term terms can be approximated to 0 compared to the lift term as the aircraft will fly in the subsonic incompressible regime. This also is already done for Equation 45 (which is derived by differentiating Equation 1 w.r.t $\hat{u}$), where the drag terms are neglected. The aforementioned C_{L_M} derivative and C_{T_u} were found in [14], where for the latter the constant power case is taken.

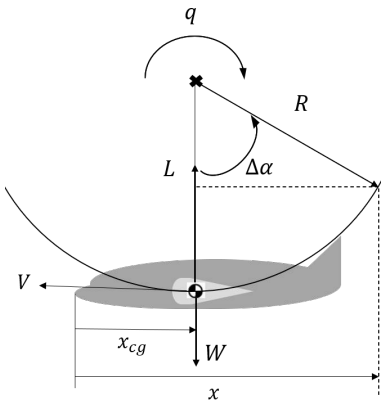

Fig. 14 Simplified representation of an idealised pull-up manoeuvre with velocity V, radius R and pitch rate q for a generic aircraft.

3. Angle of attack stability derivatives

The derivatives can be found in Equation 46 and Equation 47.

$$C_{X_\alpha} = C_{L_\alpha}\alpha_0 + C_{L,0} - C_{D_\alpha} + C_{T_\alpha} \tag{46}$$

$$C_{Z_\alpha} = -C_{L_\alpha} - C_{D_\alpha}\alpha_0 - C_{D,0} \tag{47}$$

where it is assumed that thrust is not a function of the angle of attack leading to $C_{T_\alpha} = 0$. For C_{m_α}, the equation is already derived and can be found in Equation 5.

4. Pitch rate stability derivatives

A general estimate for the change in geometric angle of attack must be first done in order to estimate the required stability derivatives C_{Z_q} and C_{m_q} whose effects are dominant during a pull-up manoeuvre. It is also essential to mention that the forward force term C_{X_q} is usually neglected as seen in both [11, 14], leading to $C_{X_q} \approx 0$.

For an idealised pull-up manoeuvre several aspects are assumed. First, the velocity V and the load factor n is assumed to be constant. Secondly, it is assumed that the aircraft motion follows a perfect circle with a radius R, assumed to be significantly larger than the size of the aircraft. The general situation can be portrayed in Figure 14.

The change in geometric angle of attack can be estimated by Equation 48, which again assumes that R is significantly larger than the overall length of the aircraft and uses the small angle approximation. Additionally, the radius R can be expressed as a function of the pitch rate q and velocity V with $R = V/q$. From the latter, Equation 48 can be rewritten into Equation 49.

$$\Delta\alpha \approx sin(\Delta\alpha) = \frac{x - x_{cg}}{R} \tag{48}$$

$$\Delta\alpha = \frac{(x - x_{cg})}{\bar{c}} \cdot \frac{q\bar{c}}{V_0} \tag{49}$$

Having derived the general equation for the change in angle of attack, it is now possible to estimate the stability derivatives of the down normal force and pitching moment defined as C_{Z_q} and C_{m_q} respectively.

For the latter, the approximation $C_Z \approx -C_L$ and the change in lift due to the pitch rate q can be used as seen in Equation 50.

$$\Delta C_L = -C_{L_{\alpha_{fwd}}} \cdot \frac{(x_{cg} - x_{ac_{fwd}})}{\bar{c}} \cdot \frac{S_{fwd}}{S} \cdot \frac{q\bar{c}}{V_0} + C_{L_{\alpha_{rear}}} \cdot \frac{S_{rear}(x_{ac_{rear}} - x_{cg})}{S\bar{c}} \left(\frac{V_r}{V}\right)^2 \cdot \frac{q\bar{c}}{V_0} \tag{50}$$

The derivative can hence be identified which leads to:

$$C_{Z_q} \approx C_{L_{\alpha_{fwd}}} \cdot \frac{(x_{cg} - x_{ac_{fwd}})}{\bar{c}} \cdot \frac{S_{fwd}}{S} - C_{L_{\alpha_{rear}}} \cdot \frac{(x_{ac_{rear}} - x_{cg})}{\bar{c}} \cdot \frac{S_{rear}}{S} \left(\frac{V_r}{V}\right)^2 \tag{51}$$

From the latter, the moment coefficient derivative is as follows:

$$C_{m_q} \approx -\left(C_{L_{\alpha_{fwd}}} \cdot \frac{S_{fwd}(x_{cg} - x_{ac_{fwd}})^2}{S\bar{c}^2} + C_{L_{\alpha_{rear}}} \cdot \frac{S_{rear}(x_{ac_{rear}} - x_{cg})^2}{S\bar{c}^2} \left(\frac{V_r}{V}\right)^2\right) \tag{52}$$

5. Angle of attack rate stability derivatives

These stability derivatives are due to the time difference associated to the front wing downwash which affects the rear wing. The latter alters the lift force on the rear wing and hence also the pitching moment. These derivatives are defined with the dimensionless change of angle of attack $\frac{\dot{\alpha}\bar{c}}{V_0}$. The effect on the vehicle drag can be neglected [14], which leads to $C_{X_{\dot{\alpha}}} \approx 0$.

In order to find an analytical estimate of the rest of the derivatives, first the time difference that the flow takes between both wings can be approximated in Equation 53 and the downwash can hence be linearised and computed with Equation 54 [14].

$$\Delta t \approx \frac{(x_{ac_{rear}} - x_{ac_{fwd}})}{V_0} = \frac{l_w}{V_0} \tag{53}$$

$$\epsilon(t) \approx \left[\epsilon_0 + \frac{d\epsilon}{d\alpha} \cdot (\alpha - \dot{\alpha}\Delta t)\right] \tag{54}$$

The additional lag term can be identified and accounted for with the aid of the product rule $\frac{d\alpha}{d\dot{\alpha}\bar{c}/V_0} = \frac{d\epsilon}{d\alpha}\frac{l_w}{\bar{c}}$ which leads to the following:

$$C_{Z_{\dot{\alpha}}} = -C_{L_{\alpha_{rear}}} \cdot \frac{S_{rear}}{S} \cdot \left(\frac{V_r}{V}\right)^2 \cdot \frac{d\epsilon}{d\alpha}\frac{l_w}{\bar{c}} \tag{55}$$

$$C_{m_{\dot{\alpha}}} = -C_{L_{\alpha_{rear}}} \cdot \frac{S_{rear}}{S} \cdot \left(\frac{V_r}{V}\right)^2 \cdot \frac{d\epsilon}{d\alpha}\frac{l_w(x_{ac_{rear}} - x_{cg})}{\bar{c}^2} \tag{56}$$

6. Side-slip stability derivatives

For the lateral motion, the derivatives of the side force Y, yaw moment N and roll moment $\mathcal{L}$ must be estimated for a small disturbance in side-slip angle β.

First, the dominant term to C_{Y_β} is from the vertical tail and can be estimated as follows:

$$C_{Y_\beta} \approx -C_{Y_{v_\alpha}} \cdot \left(1 - \frac{d\sigma}{d\beta}\right) \cdot \left(\frac{V_v}{V}\right)^2 \cdot \frac{S_v}{S} \tag{57}$$

with the different lateral parameters being already defined in subsubsection III.C.1. The yaw moment derivative, C_{n_β}, is also presented in the same section. The last stability derivative, C_{l_β} has multiple terms that depend on lift distribution, vertical tail position and wing characteristics (dihedral, quarter-chord sweep and lift curve slope) and position. These are obtained by combining a semi-empirical method from [8] for the wing contribution (corrected by a required factor, already derived in the previous section) and an approximate analytical estimate due to the vertical tail. The result is:

$$C_{l_\beta} = \sum_{w=1}^{2}\left[-\frac{C_{L_{\alpha_w}}\Gamma_w}{4} \cdot 2/3\frac{1+2\lambda_w}{1+\lambda_w} - 1.2\frac{\sqrt{AR_w}Z_{wf}(l_{fus}+w_{fus})}{b_w^2}\right]\frac{S_w b_w}{Sb}\left(\frac{V_w}{V}\right)^2 + C_{Y_{\beta_v}} \cdot \frac{z_v}{b} \tag{58}$$

where the first term is the component for both wings and accounts for the wing and wing-fuselage interference, obtained from [8]. Due to the dual-wing nature of the aircraft, this interference is averaged per wing with the term $\frac{S_w b_w}{Sb}$. Γ_w is the dihedral angle of the wing and Z_{wf} is the distance above the centre line of the wing. Indeed, a high wing has a negative contribution to the derivative, which hence is stabilising. The final component is due to the vertical moment arm, z_v, from the aerodynamic centre of the vertical tail to the CG of the aircraft. The latter assumes a small initial angle of attack, α_0.

7. Roll rate stability derivatives

The dimensionless roll rate $\frac{pb}{2V_0}$ stability derivatives are C_{Y_p}, C_{l_p} and C_{n_p}. In order to understand why all the lateral aerodynamic forces and moments change due to a roll rate, it can be understood by a change in the geometric angle of attack (as it is seen for the pitch rate). This change in angle of attack for the vertical tail can be estimated as $\Delta\alpha_v \approx \frac{pz}{V_0} = \frac{z}{b} \cdot \frac{pb}{2V_0}$ and for the wing it is $\Delta\alpha = \frac{2y}{b} \cdot \frac{pb}{2V_0}$.

First, for the side force derivative the dominant term is due to the vertical tail. Due to the 0.4 vertical tail taper ratio, the side force distribution can be approximated to be elliptical on the vertical tail. Hence, using [14], the equation is as follows:

$$C_{Y_p} \approx (C_{Y_p})_v = -\frac{8}{3\pi}\left(\frac{V_v}{V}\right)^2 \cdot \frac{b_v S_v}{bS} \cdot C_{L_{\alpha_v}} \tag{59}$$

The second derivative is C_{l_p} and it is due to a span-wise change in the sectional lift distribution. It has already been estimated previously when sizing the aileron (see subsubsection III.C.3).

Finally, the yaw moment also changes with the roll rate and can be estimated with:

$$C_{n_p} \approx -\frac{l_v}{b} \cdot (C_{Y_p})_v - \frac{1}{8}\left(C_{L_{fwd,0}} \frac{S_{fwd} b_{fwd}}{Sb} + C_{L_{rear,0}} \frac{S_{rear} b_{rear}}{Sb}\left(\frac{V_r}{V}\right)^2\right) \tag{60}$$

where the first contribution is due to the vertical tail and the second one is due to the wings. Due to the angle of attack change, the sectional drag varies along the wing as $\Delta C_d = -(C_{l,0} + C_{d_\alpha}) \cdot \Delta\alpha \approx -C_{l,0} \frac{py}{b} \frac{pb}{2V_0}$. Hence this difference in the $X-$ force along the wing, when integrated over the whole span results in an induced yaw moment (using simple strip theory). An approximation of the integral associated to the tandem wing correction can be seen as the second term of Equation 60.

8. Yaw rate stability derivatives

The last set of stability derivatives are due to a yaw rate $\frac{rb}{2V_0}$, and are the following: C_{Y_r}, C_{l_r} and C_{n_r}. In the same manner as for a pitch rate, a yaw rate induces a change in the geometric angle of attack for all the aircraft's lifting surfaces. This change in angle of attack, is $\Delta\alpha_r = \frac{(x - x_{cg})r}{V_0}$.

With the aforementioned explained, it is now possible to find analytical equations for the three stability derivatives. In a similar manner than for the roll rate derivative, C_{Y_r} represents the change in side force due to an induced change in angle of attack, and its main contribution is due to the vertical tail. This can be written as:

$$C_{Y_r} = 2 \cdot C_{Y_{v_\alpha}} \cdot \frac{S_v l_v}{Sb} \cdot \left(\frac{V_v}{V}\right)^2 \tag{61}$$

The roll moment derivative follows from the previous equations and can be written as follows:

$$C_{l_r} = \frac{z_v}{b} \cdot C_{Y_r} + \frac{1}{4} \cdot \left(C_{L_{fwd,0}} \frac{S_{fwd} b_{fwd}}{Sb} + C_{L_{rear,0}} \frac{S_{rear} b_{rear}}{Sb}\left(\frac{V_r}{V}\right)^2\right) \tag{62}$$

where the first term is due to the vertical tail (assuming a small initial angle of attack) and the second term is related to the induced change in lift due to a yaw rate (equivalent to a change in angle of attack) which consequently creates a roll moment. The latter equation is an approximation of the integral from simple strip theory by assuming an elliptical distribution of lift over the wing.

The final stability derivative can be estimated using:

$$C_{n_r} = -\frac{l_v}{b} \cdot C_{Y_r} - \frac{1}{4} \cdot \left(C_{D_{fwd,0}} \frac{S_{fwd} b_{fwd}}{Sb} + C_{D_{rear,0}} \frac{S_{rear} b_{rear}}{Sb}\left(\frac{V_r}{V}\right)^2\right) \tag{63}$$

where a similar pattern emerges with the first term being due to the vertical tail and the second being an approximation using simple strip theory of the wing contributions.

Table 4 Definitions and derived equations of the control derivatives.

Control Derivative	Equation
$C_{X_{\delta_e}} = \frac{dC_X}{d\delta_e}$	$C_{X_{\delta_e}} = 0$ [11]
$C_{Z_{\delta_e}} = \frac{dC_Z}{d\delta_e}$	$C_{Z_{\delta_e}} = \sum_{i=1}^{2}(-1)^i \tau_e \cdot \frac{S_i}{S}\frac{b_e}{b_i} \cdot C_{L_{\alpha_i}} \cdot \left(\frac{V_i}{V}\right)^2$
$C_{m_{\delta_e}} = \frac{dC_m}{d\delta_e}$	$C_{m_{\delta_e}} = -\sum_{i=1}^{2} \tau_e \cdot \frac{S_i}{S}\frac{b_e}{b_i} \cdot C_{L_{\alpha_i}} \cdot \frac{\lvert x_{cg} - x_{ac_i} \rvert}{\bar{c}}$
$C_{Y_{\delta_a}} = \frac{dC_Y}{d\delta_a}$	$C_{Y_{\delta_a}} = 0$ [11]
$C_{l_{\delta_a}} = \frac{dC_l}{d\delta_a}$	$C_{l_{\delta_a}} = \sum_{i=1}^{2} -\frac{C_{L_{\alpha_i}} \tau_a c_{r_i}}{S_i b_i} \cdot \left[\frac{y^2}{2} + \frac{2}{3}\frac{\lambda_i - 1}{b_i} y^3\right]_{b_2}^{b_1} \frac{S_i b_i}{Sb}\left(\frac{V_i}{V}\right)^2$
$C_{n_{\delta_a}} = \frac{dC_n}{d\delta_a}$	$C_{n_{\delta_a}} = -0.2 \cdot C_{L,0} \cdot C_{l_{\delta_a}}$ [8]
$C_{Y_{\delta_r}} = \frac{dC_Y}{d\delta_r}$	$C_{Y_{\delta_r}} = C_{L_{v_\alpha}} \cdot \frac{S_v}{S} \cdot \tau_r \cdot \frac{b_r}{b_v}$
$C_{l_{\delta_r}} = \frac{dC_l}{d\delta_r}$	$C_{l_{\delta_r}} = \frac{z_v}{b} \cdot C_{L_{v_\alpha}} \cdot \frac{S_v}{S} \cdot \tau_r \cdot \frac{b_r}{b_v}$
$C_{n_{\delta_r}} = \frac{dC_n}{d\delta_r}$	$C_{n_{\delta_r}} = -C_{L_{v_\alpha}} \cdot \frac{S_v l_v}{Sb} \cdot \tau_r \cdot \frac{b_r}{b_v}$ [16]

9. Control derivatives

Having designed the aerodynamic control surfaces for cruise, the aircraft's control properties are described by the aid of control derivatives. These are the changes in the aerodynamic loadings due to deflections in elevator δ_e (for longitudinal control), aileron δ_a and rudder δ_r (for lateral and directional control). These are summarised in Table 4.

A number of observations can be noted in the expressions of the control derivatives. First, the $X-$ and $Y-$ control derivatives to elevator and aileron deflection, respectively, are zero. This is approximation found in literature and can be safely assumed as a preliminary estimate. The second concept which is recurrent in the expression of the control derivatives is τ which refers to the control surface effectiveness and is already defined previously. This term allows to see how effective the aerodynamic control surface (for a change in deflection) are when translated to a local increase in lift (or side-force). Thirdly, it must be understood that the elevator and aileron are placed on both wings of the aircraft (analogous to an aircraft with both a canard and a tail for the elevator), leading to the summing nature of the elevator control derivative derived from Equation 31 and roll control derivative equations. Finally, for $C_{l_{\delta_a}}$, the equation is derived and corrected with a combined method using strip theory [20] and [18], as explained in subsubsection III.C.3.

10. Results and specific consideration for lateral open-loop stability

The stability and control derivatives obtained in this section are summarised in Table 5.

Table 5 Summarised stability and control derivatives for both longitudinal and lateral motion for clean cruise configuration.

Longitudinal Force Derivatives	**Normal Force Derivatives**	**Pitch Moment Derivatives**
C_{X_u} = -0.16374	$C_{Z_u} = -0.024899$	$C_{m_u} = 0.0061871$
$C_{X_\alpha} = 0.2487$	$C_{Z_\alpha} = -3.6501$	$C_{m_\alpha} = -0.1320$
$C_{X_{\dot{\alpha}}} = 0$	$C_{Z_{\dot{\alpha}}} = -3.6320$	$C_{m_{\dot{\alpha}}} = -10.0364$
$C_{X_q} = 0$	$C_{Z_q} = -2.4294$	$C_{m_q} = -22.9669$
$C_{X_{\delta_e}} = 0$	$C_{Z_{\delta_e}} = 0$	$C_{m_{\delta_e}} = -3.8147$
Lateral Force Derivatives	**Roll Moment Derivatives**	**Yaw Moment Derivatives**
$C_{Y_\beta} = -0.1443$	$C_{l_\beta} = -0.05192$	$C_{n_\beta} = 0.05404$
$C_{Y_{\dot{\beta}}} = 0$		$C_{n_{\dot{\beta}}} = 0$
$C_{Y_p} = -0.02243$	$C_{l_p} = -0.7462$	$C_{n_p} = -0.02082$
$C_{Y_r} = 0.1469$	$C_{l_r} = 0.1585$	$C_{n_r} = -0.08167$
$C_{Y_{\delta_a}} = 0$	$C_{l_{\delta_a}} = -0.09817$	$C_{n_{\delta_a}} = 0.01013$
$C_{Y_{\delta_r}} = 0.8693$	$C_{l_{\delta_r}} = 0.1746$	$C_{n_{\delta_r}} = -0.4423$

For lateral motions, the stability derivatives C_{n_β} and C_{l_β} define the lateral stability behaviour in terms of Dutch Roll convergence and spiral stability. The spiral stability limit is determined by the equation:

$$E = C_{L,0} \cdot (C_{l_\beta} \cdot C_{n_r} - C_{n_\beta} \cdot C_{l_r}) = 0 \tag{64}$$

For Dutch Roll stability is determined by the Routh's Discriminant which should be positive:

$$R(C_{l_\beta}, C_{n_\beta}) = B \cdot C(C_{l_\beta}, C_{n_\beta}) \cdot D(C_{l_\beta}, C_{n_\beta}) - A \cdot (D(C_{l_\beta}, C_{n_\beta}))^2 - B^2 \cdot E(C_{l_\beta}, C_{n_\beta}) > 0 \tag{65}$$

where the relations for A, B, $D(C_{l_\beta}, C_{n_\beta})$ and $E(C_{l_\beta}, C_{n_\beta})$ can be found in [11].
Both can now be plotted in the $(-C_{l_\beta}, C_{n_\beta})$ plane and can be seen in Figure 15.

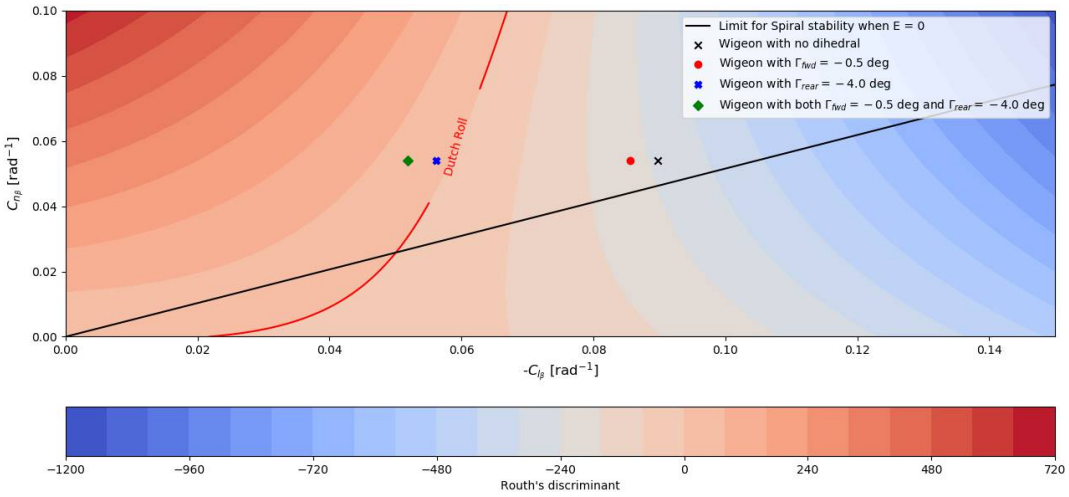

Fig. 15 Dutch roll and spiral stability limits plotted in the $(-C_{l_\beta}, C_{n_\beta})$ plane. The aircraft is represented by a dot in the plane with its initial properties, and different changes to the dihedral lead to different positions in the space.

From Figure 15, it can be seen that the specific eVTOL has both a divergent Dutch Roll and an unstable spiral. Usually, an unstable spiral can easily be dealt with by the pilot as it is a very slow motion. Dutch Roll, however, should

be stable as it can be detrimental to passenger comfort. To address the latter, the dihedral of the aircraft was changed, as it was previously explained that C_{l_β} is a function of the dihedral angle for both wings (see Equation 58). It was observed that if the dihedrals are set to $\Gamma_{fwd} = -0.5\,\text{deg}$ and $\Gamma_{rear} = -4.0\,\text{deg}$, the aircraft has a convergent Dutch Roll (with a sufficient margin to account for assumptions). The smaller forward dihedral is chosen in order to minimise the risk of the forward wing touching ground during hover or vertical flight, whereas the rear wing dihedral was limited to -4.0 deg so that it does not affect the propellers efficacy and aforementioned computations for yaw control.

E. Simulation of open-loop dynamics

The non-dimensional and linearised equations of motion of an aircraft for both symmetric and asymmetric motions have been derived in [11]. A brief overview of the derivation process applied to obtain those equations is provided in this section. The equations of motion expressed in matrix form are transformed in a state-space form in order to simulate the aircraft responses to specific disturbances and control inputs. Those equations of motion were linearised for a steady, straight, symmetric flight in the stability reference frame. This is valid for small disturbances from an initial equilibrium condition of steady, straight, symmetric flight (i.e. being the reference condition). Since the aircraft motion studied in this report was described by a set of linear equations of motion, the stability of a specified equilibrium condition is independent of the input or disturbance.

For the equations of motion the stability reference frame is adopted, where the x-axis lies in the symmetry plane and its direction is situated along the longitudinal component of the velocity of the centre of gravity. The z-axis also lies in the symmetry plane and points downwards perpendicular to the x-axis. The y-axis points out of the x-z plane as to complete the right-handed coordinate system.

The equations of motion can be rewritten into the following form:

$$\mathbf{C_1}\dot{\vec{x}} + \mathbf{C_2}\vec{x} + \mathbf{C_3}\vec{u} = \vec{0} \tag{66}$$

where $\mathbf{C}_1$, $\mathbf{C}_2$ and $\mathbf{C}_3$ are stability matrices, $\vec{x}$ is the state vector containing the required responses and $\vec{u}$ is the input vector. First, the required matrices are derived for the symmetric case, resulting in:

$$\mathbf{C_1} = \begin{bmatrix} -2\mu_c \cdot \bar{c}/V_0 & 0 & 0 & 0 \\ 0 & (C_{Z_{\dot{\alpha}}} - 2\mu_c) \cdot \bar{c}/V_0 & 0 & 0 \\ 0 & 0 & -\bar{c}/V_0 & 0 \\ 0 & C_{m_{\dot{\alpha}}} \cdot \bar{c}/V_0 & 0 & -2\mu_c \cdot {K_{yy}}^2 \cdot \bar{c}/V_0 \end{bmatrix} \tag{67}$$

$$\mathbf{C_2} = \begin{bmatrix} C_{X_u} & C_{X_\alpha} & C_{Z_0} & C_{X_q} \\ C_{Z_u} & C_{Z_\alpha} & -C_{X_0} & (C_{Z_q} + 2\mu_c) \\ 0 & 0 & 0 & 1 \\ C_{m_u} & C_{m_\alpha} & 0 & C_{m_q} \end{bmatrix} \tag{68}$$

$$\mathbf{C_3} = \begin{bmatrix} C_{X_{\delta_e}} \\ C_{Z_{\delta_e}} \\ 0 \\ C_{m_{\delta_e}} \end{bmatrix} \tag{69}$$

where in the symmetric case, the state vector, $\vec{x} = [\hat{u}\ \alpha\ \theta\ q\bar{c}/V_0]^T$ and $\vec{u}$ is equal to the elevator deflection δ_e.

Second, the same procedure is performed for the asymmetric case resulting in the following:

$$\mathbf{C_1} = \begin{bmatrix} (C_{Y_{\dot{\beta}}} - 2\mu_b) \cdot b/V_0 & 0 & 0 & 0 \\ 0 & -\frac{1}{2} \cdot b/V_0 & 0 & 0 \\ 0 & 0 & -4\mu_b K_{xx}^2 \cdot b/V_0 & 4\mu_b \cdot K_{xz} \cdot b/V_0 \\ C_{n_{\dot{\beta}}} \cdot b/V_0 & 0 & 4\mu_b \cdot K_{xz} \cdot b/V_0 & -4\mu_b K_{zz}^2 \cdot b/V_0 \end{bmatrix} \tag{70}$$

$$\mathbf{C_2} = \begin{bmatrix} C_{Y_\beta} & C_{L,0} & C_{Y_p} & (C_{Y_r} - 4\mu_b) \\ 0 & 0 & 1 & 0 \\ C_{l_\beta} & 0 & C_{l_p} & C_{l_r} \\ C_{n_\beta} & 0 & C_{n_p} & C_{n_r} \end{bmatrix} \tag{71}$$

$$\mathbf{C_3} = \begin{bmatrix} C_{Y_{\delta_a}} & C_{Y_{\delta_r}} \\ 0 & 0 \\ C_{l_{\delta_a}} & C_{l_{\delta_r}} \\ C_{n_{\delta_a}} & C_{n_{\delta_r}} \end{bmatrix} \tag{72}$$

where for the asymmetric case $\vec{x} = [\beta\ \phi\ pb/(2V_0)\ rb/(2V_0)]^T$ and $\vec{u} = [\delta_a\ \delta_r]^T$, where δ_a and δ_r are functions of time or are input to the model as arrays.

The final step requires transforming the matrices $\mathbf{C}_1$, $\mathbf{C}_2$ and $\mathbf{C}_3$ into the state-space matrices **A**, **B**, **C** and **D** in the following:

$$\dot{\vec{x}} = \mathbf{A}\vec{x} + \mathbf{B}\vec{u} \;\; \& \;\; \vec{y} = \mathbf{C}\vec{x} + \mathbf{D}\vec{u} \tag{73}$$

where $\vec{y}$ is the output vector which is chosen to be equal to $\vec{x}$, resulting in **C** being the identity matrix and **D** being a matrix containing only zeroes.

The computation of **A** and **B** is implemented using Equation 74.

$$\mathbf{A} = -\mathbf{C_1}^{-1}\mathbf{C_2} \;\; \& \;\; \mathbf{B} = -\mathbf{C_1}^{-1}\mathbf{C_3} \tag{74}$$

The latter results in $\mathbf{A}_s$ for the symmetric case and $\mathbf{A}_a$ for the asymmetric case.

It can be seen that a set of additional inputs are required. These inputs are the aircraft's non-dimensional inertia are as follows: $K_{xx}^2 = \frac{I_{xx}}{mb^2}$, $K_{yy}^2 = \frac{I_{yy}}{m\bar{c}^2}$, $K_{zz}^2 = \frac{I_{zz}}{mb^2}$ and $K_{xz} = \frac{I_{xz}}{mb^2}$. The final aerodynamic inputs to the state-space system are $C_{L,0}$, C_{X_0} and C_{Z_0} computed as follows:

$$C_{X_0} = \frac{Wsin(\theta_0)}{1/2\rho V_0^2 S} \tag{75}$$

$$C_{Z_0} = \frac{-Wcos(\theta_0)}{1/2\rho V_0^2 S} \tag{76}$$

which require the weight W, the airspeed V_0, the air density ρ and finally θ_0 which is the initial pitch angle. Finally, the non-dimensional mass μ_c and μ_b must be computed using:

$$\mu_c = \frac{W}{g\rho S\bar{c}} \tag{77}$$

$$\mu_b = \frac{W}{g\rho Sb} \tag{78}$$

Using the stability and control derivatives given in Table 5, the values for the state-space matrices can be computed. Based on this, the poles and zeroes of both the symmetric and asymmetric state-space system are found. They are displayed in Figure 16.

In the symmetric system, all poles have negative real parts, meaning that they are open-loop stable. There is one periodic eigenmode (pair of complex poles) and two aperiodic eigenmodes (real poles). This is in contrast to conventional aircraft, which have two periodic symmetric eigenmodes. In the asymmetric system, there is again one periodic eigenmode and two aperiodic modes. This is the same as for conventional aircraft, where the Dutch roll, the aperiodic roll and spiral modes are observed. The spiral mode is unstable for the Wigeon (as for many conventional aircraft), but the other eigenmodes are stable.

This behaviour is favourable in the sense that the aircraft is stable in all modes except the spiral, which can be deemed acceptable due to it being very slow. However, while stability is an essential criterion for controlling an aircraft, it is not the only one. As Figure 17 shows, a small step input to the elevator (a typical input given by a pilot to change the pitch angle) results in a very large change in V and θ. Furthermore, the response is very slow to settle on its final value, with a large overshoot in all state variables. This needs to be addressed with a closed-loop fly-by-wire system.

Figure 18 shows the response of the asymmetric states to a pulse-shaped rudder input. The Dutch Roll mode causes high-frequency oscillations in all states, while the unstable spiral mode causes a slow divergence that is especially visible in the roll angle and yaw rate. Since the Dutch roll is very unpleasant for the occupants of an aircraft and can cause nausea, it is essential that the oscillations are reduced.

Finally, Figure 19 shows the response of the aircraft states to a pulse-shaped aileron input. The responses are qualitatively similar as for the rudder, except for an initial peak in p, which is the primary function of the aileron. Furthermore, the magnitude of the response is smaller.

It has therefore been established that a controller is required to achieve good handling qualities of the aircraft in cruise. It needs to decrease the response time and overshoot for the elevator response, reduce the oscillations of the Dutch roll and potentially eliminate the instability due to the spiral mode.

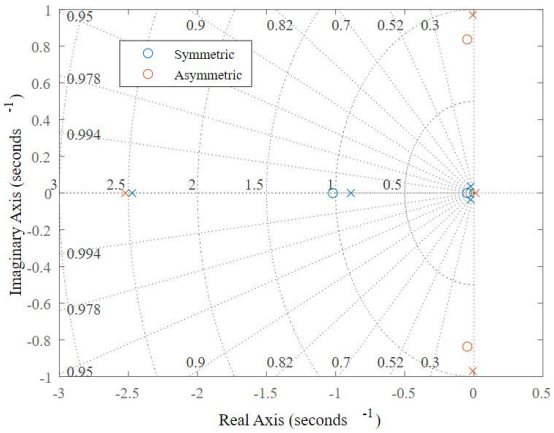

Fig. 16 Map of the open-loop poles and zeroes of the aircraft in cruise. Crosses indicate poles, circles indicate zeroes.

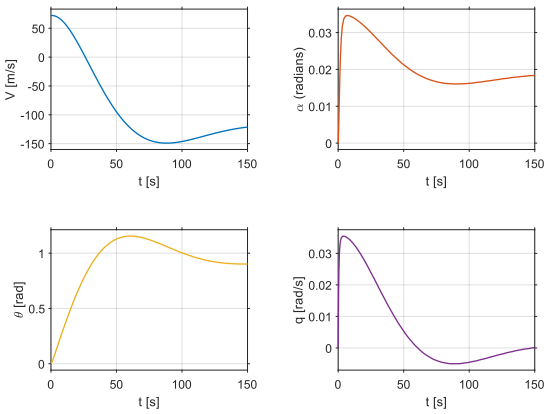

Fig. 17 Open-loop response of the airspeed V, the angle of attack α, the pitch angle θ, and the pitch rate q to a step elevator input of -0.005 rad.

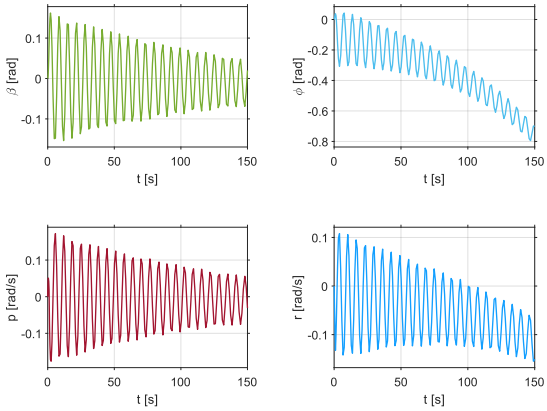

Fig. 18 Open-loop response of the sideslip angle β, the roll angle ϕ, the roll rate p, and the yaw rate r to a pulse rudder input of 0.025 rad (for 1 second).

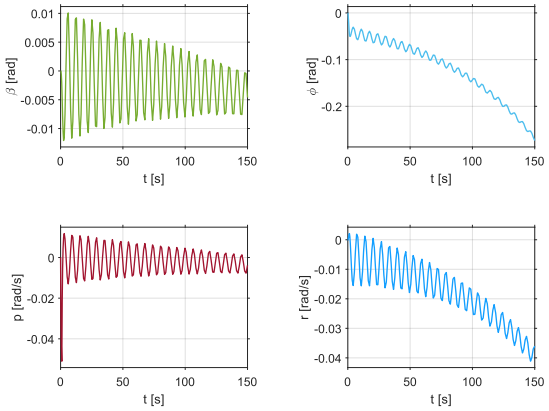

Fig. 19 Open-loop response of the sideslip angle β, the roll angle ϕ, the roll rate p, and the yaw rate r to a pulse rudder input of 0.025 rad (for 1 second).

F. Controller design

In this section, the design of a closed-loop controller for the Wigeon is described. The purpose of this controller is to improve on the open-loop dynamics of the eVTOL in terms of stability and handling quality. Since the Wigeon spends most of its mission time in cruise, the present study focuses on a controller to make the aircraft easy to fly in cruise. The design of controllers for VTOL operation and the transition phase are beyond the scope of this preliminary design method.

1. Control allocation

In order to introduce the controller design, it is essential to qualitatively mention the required control allocation.

It is important to know what the pilot commands are and how these commands can be translated to deflections of the aerodynamic surfaces or varying angular speed of the propellers. For cruise, a control stick for pitch, a side stick for roll and pedals for yaw are connected to a flight control system that directly controls the deflections of the control surfaces (through the use of actuators) and corrects accordingly for any instabilities. The pilot can therefore set a certain attitude angle for pitch and a target heading angle for yaw control which automatically sets a roll rate for roll control when a certain turn manoeuvre must be performed, where for the roll rate a certain maximum bank angle is allowed within the

flight envelope. Finally, to control the aircraft during hover, a collective lever will be used by the pilot which modulates the speed of the propellers *. Additionally, pedals can be used by the pilot to control the rudder, as in for cruise, and during ground operations it can be used as differential braking.

2. Controller architecture and closed-loop dynamics

A high-level overview of the controller architecture (created in Simulink) can be seen in Figure 20. While the pitch controller only consists of one feedback loop with a PI (proportional integral) controller, the lateral controller is more sophisticated. It is inspired by a lecture by How [21] on a controller for coordinated turns.

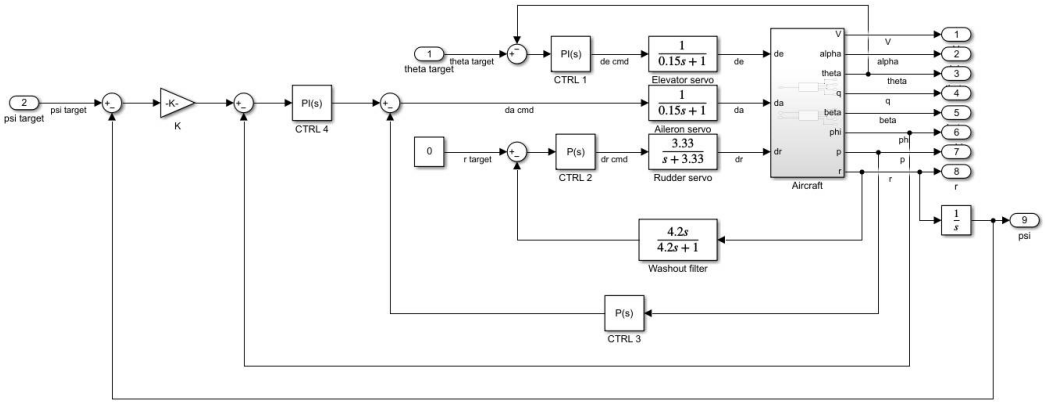

Fig. 20 Architecture of the controller for cruise.

In order to improve the Wigeon's longitudinal dynamics a feedback loop from the pitch angle θ is used. The pilot sets a target pitch angle θ_{target}, which is compared to the current pitch angle (measured by an inertial measurement unit) and then fed through a PI controller. The dynamics of the elevators are modelled using the transfer function $\frac{1}{0.15s+1}$, which is the transfer function proposed by [21] for the aileron. Modelling the elevator as a transfer function takes into account that its response speed is limited and occurs with a delay.

After tuning the controller gains with Simulink's PID tuner app, the resulting gain and phase margins are 22.3 dB and 147 degrees, as seen in Figure 21. The step responses of the longitudinal states to a step input to θ_{target} is shown in Figure 22. It can be seen that the aircraft is not only stable, but also responds quickly with minimal overshoot.

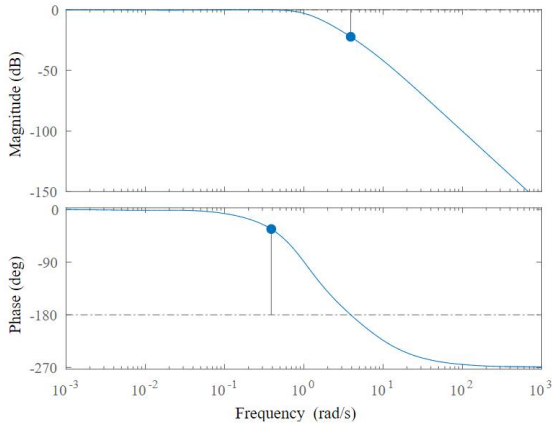

Fig. 21 Bode plot of the closed-loop response of θ to θ_{target} set by the pilot.

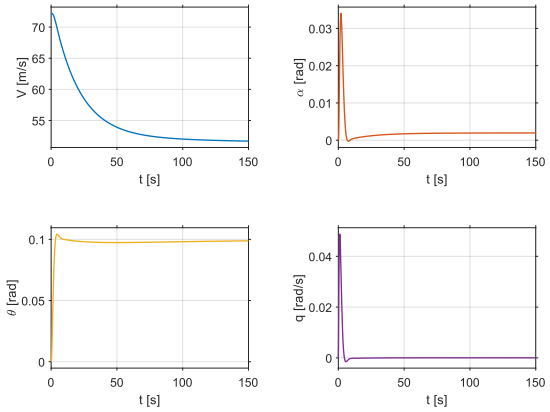

Fig. 22 Closed-loop response of the airspeed V, the angle of attack α, the pitch angle θ, and the pitch rate q to a step input of 0.1 rad to θ_{target}.

*URL https://evtol.com/features/behind-the-controls-of-an-evtol-aircraft-a-test-pilots-perspective/ [cited 15 June 2021]

The lateral controller is structured as described by How [21] for a lateral controller that takes a heading input and performs coordinated turns. A gain K calculates the appropriate roll angle ϕ based on the error in the yaw angle ψ. The error in the yaw angle is then fed through a controller block, whose output is compared to the roll rate which has a gain (proportional controller) applied. The output of this comparison is fed as a command to the aileron actuator. At the same time, another feedback loop with a washout filter on the yaw rate attempts to bring the yaw rate to zero. This is the yaw damper designed to reduce low-frequency oscillations (Dutch roll).

The aileron and rudder actuators are modelled as $\frac{1}{0.15s+1}$ and $\frac{3.33}{s+3.33}$, respectively. In order to reduce oscillations in the response, a PI controller was used for CTRL 4 in Figure 20 instead of the proportional controller in the original work.

In Figure 23, the Bode plot showing the response of the heading angle ψ to the pilot input ψ_{target} is shown. The system is closed-loop stable with a gain margin of 12.4 dB and a phase margin of -180 degrees. These margins are not as good as for the longitudinal case, so there is further room for optimisation. This is confirmed by the step responses shown in Figure 24 are also slower and more oscillatory than for the longitudinal controller.

In Figure 25, the poles and zeroes of the open-loop system can be seen. All poles are now stable (with a negative real part), which is an improvement over the open-loop system in Figure 16. However, the asymmetric system now has two zeroes in the right half-plane. This can lead to the system's initial response being in the opposite direction of its final value. This can, in fact, be observed in the evolution of r in Figure 24. This confirms that in future iterations of the design, the lateral controller may have to be reviewed to improve handling qualities.

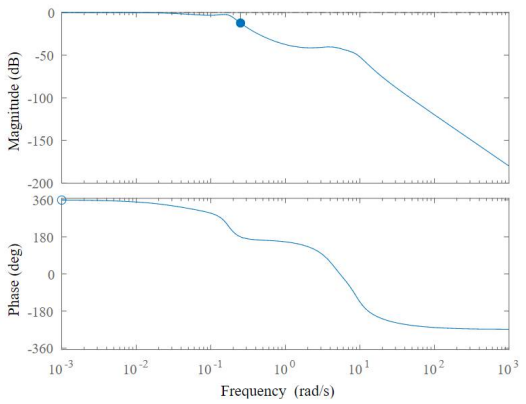

Fig. 23 Bode plot of the closed-loop response of ψ to ψ_{target} set by the pilot.

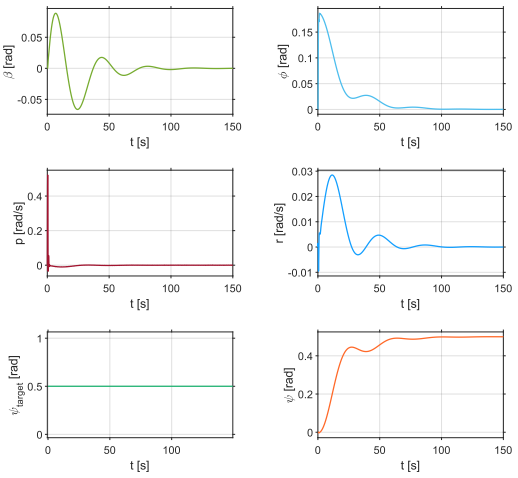

Fig. 24 Closed-loop response of the sideslip angle β, the roll angle ϕ, the roll rate p, the yaw rate r, and the yaw angle ψ to a step input of 0.5 rad to ψ_{target}.

IV. Controllability in hover

In hover mode, the oncoming airspeed experienced by the vehicle is very low. Therefore, aerodynamic control surfaces are not an effective means of control and thrust vectoring and differential thrust must be used. In order to quantify the controllability of the eVTOL in hover, the Available Control Authority Index (ACAI) developed by Du et al. [22] is used. The ACAI is designed to evaluate available control authority of hovering multirotor vehicles with fixed rotors. While the Wigeon can tilt its rotors (by tilting the wings), neglecting this possibility for hover control simplifies the analysis considerably while also being conservative.

Du et al. [22] model the dynamics of a hovering multicopter using a state-space system of the form given in Equation 79. 8 states are considered, which are given in Equation 80. These include the altitude h, the roll angle ϕ, the pitch angle θ, the yaw angle ψ, the vertical speed v_h, the roll rate p, the pitch rate q, and the yaw rate r. Equation 81 shows the control variables, which are the total thrust force T, the roll moment N, the pitch moment M, and the yaw moment L. The weight $m_a \cdot g$ is also included in this vector for the sake of convenience.

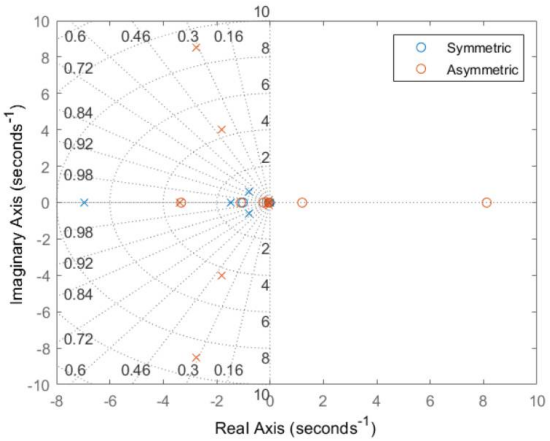

Fig. 25 Map of the closed-loop poles and zeroes of the aircraft in cruise. Crosses indicate poles, circles indicate zeroes.

$$\dot{\boldsymbol{x}} = A\boldsymbol{x} + B\boldsymbol{u} \tag{79}$$

$$\boldsymbol{x} = \begin{bmatrix} h & \phi & \theta & \psi & v_h & p & q & r \end{bmatrix}^T \tag{80}$$

$$\boldsymbol{u} = \boldsymbol{F} - \boldsymbol{G} = \begin{bmatrix} T & L & M & N \end{bmatrix}^T - \begin{bmatrix} m_a \cdot g & 0 & 0 & 0 \end{bmatrix}^T \tag{81}$$

According to Du et al. [22], there are two necessary and sufficient conditions for multirotor controllability in hover:
1) rank $C(A, B) = 8$
2) ACAI > 0

$C(A, B)$ is defined by Equation 82, where A and B are the state and input matrices of the state-space system in Equation 79. However, this condition was not found to be limiting for the eVTOL under any condition.

$$C(A, B) = \begin{bmatrix} B & AB & A^2B & \dots & A^7B \end{bmatrix} \tag{82}$$

The procedure for calculating the ACAI is described in [22] in detail. The calculation is implemented in Python using the Matlab Toolbox [23] developed by Du et al. [22] as an example and means of verification. At this point, only the inputs required to perform the calculation are listed in Table 6. Note that since the origin of the coordinate system is the centre of mass, this is also implicitly an input to the calculation.

Table 6 Input parameters to the calculation of the ACAI [22].

Parameter	Description
$x_1, x_2, \dots, x_m$	x-position of each rotor w.r.t the centre of mass
$y_1, y_2, \dots, y_m$	y-position of each rotor w.r.t the centre of mass
$K_1, K_2, \dots, K_m$	Maximum thrust of each rotor
k_μ	Ratio between reactive torque and thrust of a rotor
$w_1, w_2, \dots, w_m$	Direction of rotation of each rotor
$\eta_1, \eta_2, \dots, \eta_m$	Efficiency parameter of each rotor
m_a	Vehicle mass

In order to calculate the ACAI of the eVTOL, it is assumed that the rotors are located at 0.5 m and 6.1 m from the aircraft nose (for the front and rear wing, respectively), and evenly spaced between 1.0 m and 4.1 m outwards from the symmetry plane. The parameter k_μ is assumed to be 0.1 based on the values used by Du et. al [22]. As for the direction of rotation of the propellers, they are all taken to be rotating inboard.

Using these values, along with the MTOM and the maximum thrust per rotor, an ACAI of 350.0 is obtained. Since this is positive, the aircraft is controllable. However, the design is not the most efficient design possible for hover, since the forward CG location causes the front rotors to be more loaded in hover.

This was highlighted in a sensitivity study conducted to understand the influence of different parameters. Figure 26 shows the dependency of the ACAI is on the centre of gravity location x_{cg}. The best controllability is achieved when the centre of gravity lies in the middle between the wings. The Wigeon's centre of gravity lies in front of this, leading to suboptimal performance. Due to this, the ACAI of the Wigeon increases when the front wing is moved forward, away from the centre of gravity (which gives them a larger moment arm).

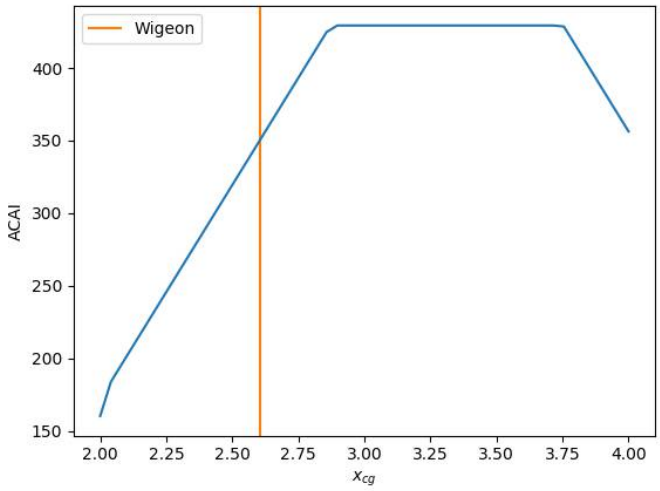

Fig. 26 Variation of the ACAI with x_{cg}.

Lateral placement of rotors also plays a role: spreading the rotors out over a larger range increases the ACAI. In other words, placing the rotors closer to the symmetry plane on one side and further towards the wingtips on the other side improves performance. Other parameters behave as expected, where a larger mass reduces the ACAI and a higher thrust increases it.

Finally, the effect of the parameter k_μ was investigated (see Figure 27). The contribution of this coefficient is crucial for yaw control, and estimating it accurately at a preliminary stage is challenging. However, variations in k_μ do not lead to uncontrollable behaviour unless $k_\mu = 0$. Its value also does not create more restrictive limits on other parameters, so finding a precise value is not necessary at a preliminary stage.

The ACAI also allows to evaluate performance after rotor failures. To model this, the efficiency factors η are set to zero for the corresponding rotors. This method can be used to ensure that hover control is failsafe.

V. Transition

Having established how the eVTOL can be made controllable both in hover and in cruise flight, it remains to be shown that the available control inputs can achieve the transition between these two flight modes. This phase of the flight is very difficult to model, so only a qualitative statement will be made in this article.

The dominant aspect of transition is the acceleration/deceleration between stall speed and zero airspeed. This is achieved by tilting the rotors between their vertical orientation in hover to a horizontal orientation in cruise flight. Due to the low airspeed, most of the control authority will be obtained from the rotors rather than aerodynamic surfaces. Therefore, it is assumed that control of other state variables than horizontal speed is achieved in the same way as in hover.

In order to design a controller for the transition phase, certain aerodynamic aspects must be taken into account. These mostly relate to the nature of the flow during transition which becomes very difficult to predict due to hysteresis. In fact, during transition, there is a sudden change from fully separated to attached flow which in turn translates to a sudden change in lift over the wings. Additionally, the modelling unpredictability is enhanced due to the phenomenon of

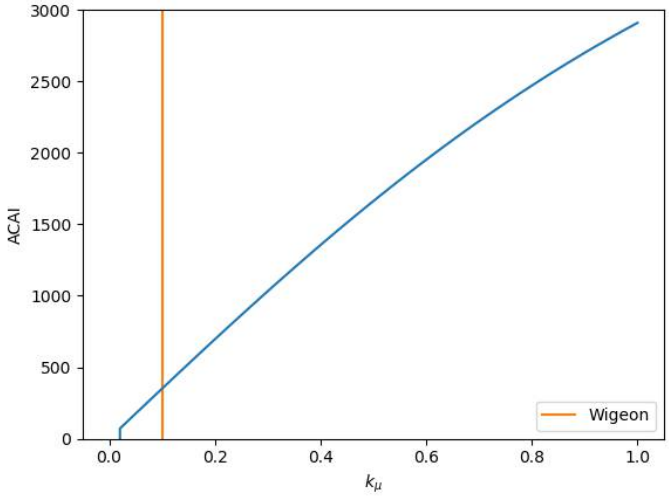

Fig. 27 Variation of the ACAI with k_μ.

hysteresis where the stalling characteristics of the aircraft depend on the flow's history. Furthermore, an unpredictable atmosphere can increase the complexity of the model, which e.g. the case of a sudden change in wind gust (whether it is a change in magnitude or direction), the flow over wings may re-attach or separate sooner/later than predicted.

For the pure transition phase itself, the controller must also be able to react accordingly for a range of different situations such as if the flow separates/(re-)attaches first at the forward wing, or if the flow first (re-)attaches/separates at the rear wing or for the rarest case that the nature of the flow changes at the same time for both wings. It can be understood that all these different situations create different and unpredictable pitching moments, that can be aggravated by an unpredictable atmosphere as explained previously. The latter introduces a dangerous transient response, which shows the need for a robust controller.

There is yet another complication: due to the high angles of attack attained during transition, there is an increased risk that the rear rotors could enter the wake of the front rotors or front wing, thereby leading to a sudden loss in thrust. The aircraft has its entire wing tilting which will create a larger wake, which is a risk that will certainly need attention.

Because of this, a quantitative analysis of transition dynamics is beyond the scope of this paper.

VI. Ground stability

The placement of the landing gear is restricted in the design of the Wigeon aircraft due to crashworthiness considerations that dictate that no stiff structure shall be located directly below human occupants [1]. Therefore, the rear landing gear is placed far aft behind the passenger cabin (at 4.76 m from the nose) and the traditional single nose gear is replaced by two gears (at 1.36 m from the nose) to be able to place them next to the pilot rather than below.

With this restriction in mind, a total of five criteria are considered. The two first among these are the maximum turn-over angle and the minimum load on the steering wheels. The former requires that the centre of gravity of the aircraft must be located at an angle of 55 degrees above the line connecting the nose wheels and the rear wheels. This criterion is originally proposed for tricycle landing gears in [5], but is extended to quadricycle landing gears, as shown in Figure 28.

The purpose of this requirement is to avoid the the eVTOL tipping over to the side while taxiing. The load criterion on the steering wheels (which are the nose wheels in the case of the Wigeon) is related to controllability [5]. It requires that at least 8% of the total aircraft weight must rest on the steering wheels for them to achieve their function.

Three additional requirements are the clearance of the wings when they are vertical, clearance of the rotors when the wings are horizontal, and the maximum tip-back angle. The last two requirements are common in conventional aircraft, but would only be relevant for emergency situations for the Wigeon. This is because in a conventional mission, it would land vertically with the rotors oriented upwards. However, it is assumed that the landing gear can tolerate a landing with wings in horizontal configuration on a regular airfield [1]. This could allow for a safe landing if the rotation mechanism

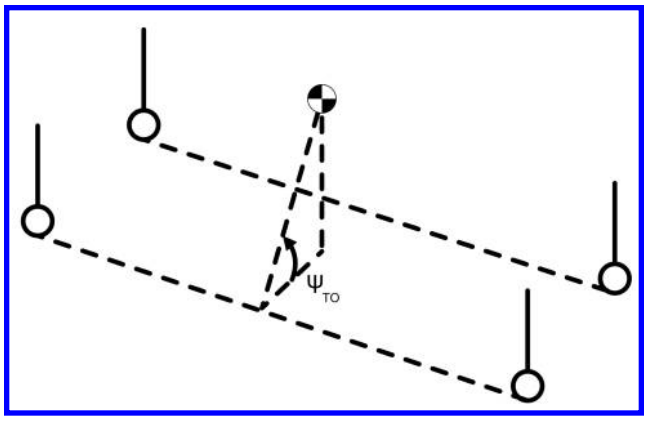

Fig. 28 Definition of the turn-over angle for a quadricycle landing gear.

of one or both wings should fail during cruise.

The critical requirement for clearance is found to be the root chord of the wing when in vertical position, dictating the required height of the landing gear. The track width of the landing gear is determined by the turn-over requirement. The corresponding equations are Equation 83 and Equation 84. Note that it is chosen to use the same track width for the front and rear wheels. This is because reducing the track width in one of them would have required an increase in the other in order to satisfy the turn-over requirement. Therefore, this design minimises the maximum track width.

$$\tan(\psi_{to}) = \frac{z_{cg} + h_{lg}}{tw/2} \qquad (83)$$

$$\tan(\phi_{cl}) = \frac{\tan(\Gamma) y_{rot} + h_{lg} + z_f - r_{rot}/2}{y_{rot} - tw/2} \qquad (84)$$

Here, ψ_{to} is the turn-over angle, z_{cg} is the z-location of the aircraft's centre of gravity, h_{lg} is the height of the landing gear, tw is the track width of the landing gear, ϕ_{cl} is the clearance angle, Γ is the front wing's dihedral, y_{rot} is the spanwise location where the wing rotates, z_f is the z-location of the front wing root chord, and r_{rot} is the maximum length of the chord behind the rotation point (i.e., radius of the circle traced by the trailing edge of the front wing when rotating). In order to increase the clearance for the rotated wing, z_f is decreased by 10 cm compared to its real value, leading to a 10 cm higher landing gear.

Solving Equations 83 and 84 for h_{lg} and tw, with the recommended values ψ_{to} = 55 degrees and ϕ_{cl} = 5 degrees from [5], and applying the additional 10 cm clearance, yields a landing gear height of 0.9278 m and a track width of 2.220 m. The track width is therefore 0.8400 m wider than the fuselage, meaning that the landing gear must be deployed 0.4200 m outboard of the fuselage.

VII. Integration of stability and control into the design process

So far, the design process for stability and control of the Wigeon has been presented in isolation, assuming that all other aircraft parameters are known. However, this is rather different from the approach taken to design the aircraft. To obtain a convergent design, the calculations from different disciplines are integrated in a single design code that allowed for a high degree of automation. In this code, an initial set of parameters is iteratively altered until all requirements are met. First, the wings are sized according to the procedure explained in subsection III.B, then hover controllability is checked to see that any one engine could fail while maintaining controllability. If this is not initially the case, the thrust-to-weight ratio is increased until the requirement is met. Then, the CG excursion is calculated and used to place the landing gear optimally, and the process monitors whether the track width does not become too high. Sizing the vertical tail and control surfaces is one of the last steps in one iteration, since they are not found to be an issue in most cases, which limits their influence on other design aspects. The simulation and controller design for cruise is done manually after a converged design had been found.

VIII. Conclusion and recommendations

This study presented a methodology for the preliminary evaluation of control and stability that is compatible with the multi-disciplinary design, analysis and optimization (MDAO) of novel aircraft systems. The methodology is herein applied in the MDAO of a tandem tilt-wing long-range eVTOL aircraft, named Wigeon. The methodology can used applied and extended for other novel aircraft concepts.

Future work should include the verification of the linearised dynamics model for cruise using more detailed simulations tools such as computational fluid dynamics (CFD). A number of CFD simulations could be performed at different angles with respect to the incoming flow to characterise the behaviour of the aircraft. Furthermore, the stability and control effects in transition manoeuvre and the corresponding governing aerodynamic equations should be further developed.

Credit authorship contribution statement

M. Cuadrat-Grzybowski, J.J. Schoser: Methodology, investigation, formal analysis, validation, software, writing - original draft preparation, writing - reviewing and editing. **S.G.P. Castro:** Conceptualization, supervision, writing - reviewing and editing.

Acknowledgments

This work has been developed as part of the Design Synthesis and Exercise "Multi-Disciplinary Design and Optimisation of a Long-Range eVTOL Aircraft", given during the Spring quarter in 2021. We would like to thank our fellow companions Javier Alba Maestre, Egon Beyne, Michael Buszek, Alejandro Montoya Santamaria, Nikita Poliakov, Koen Prud'homme van Reine, Noah Salvador López and Kaizad Wadia who are part of the team conducting this design.

Additionally, we would like to thank Davide Biagini and Dr. Ali Nokhbatolfoghahai for their generous help, advice and supervision in composing this project. We would also like to thank Dr. Erik-Jan van Kampen for providing us with guidance in the early phase of this project.

References

[1] Alba-Maestre, J., Beyne, E., Buszek, M., Cuadrat-Grzybowski, M., Montoya Santamaria, A., Poliakov, N., Prud'homme van Reine, K., Salvador Lopez, N., Schoser, J., and Wadia, K., "Final Report - Multi-Disciplinary Design and Optimisation of a Long-Range eVTOL Aircraft," Tech. rep., Delft University of Technology, 2021. https://doi.org/10.5281/zenodo.5576103.

[2] Alba-Maestre, J., Beyne, E., Buszek, M., Cuadrat-Grzybowski, M., Montoya Santamaria, A., Poliakov, N., Prud'homme van Reine, K., Salvador Lopez, N., Schoser, J., and Wadia, K., "Baseline Report - Multi-Disciplinary Design and Optimisation of Long-Range eVTOL Aircraft," Tech. rep., Delft University of Technology, 2021. https://doi.org/10.5281/zenodo.5575953.

[3] Alba-Maestre, J., Prud'homme van Reine, K., Sinnige, T., and Castro, S. G. P., "Preliminary propulsion and power system design of a tandem-wing long-range eVTOL aircraft," *Applied Sciences*, Vol. 11, No. 23, 2021. https://doi.org/10.3390/app112311083.

[4] Chauhan, S. S., and Martins, J. R., "Tilt-wing eVTOL takeoff trajectory optimization," *Journal of Aircraft*, Vol. 57, 2020, pp. 93–112. https://doi.org/10.2514/1.C035476.

[5] Torenbeek, E., *Synthesis of subsonic airplane design*, Delft University Press, 1982.

[6] Oliviero, F., "Requirement Analysis and Design Principles for AC Stability and Control (Part 1)," , 2 2021.

[7] Salvador López, N., Montoya Santamaría, A., and Castro, S. G. P., "Preliminary aerodynamic analysis for the multi-disciplinary design and optimisation of a long-range eVTOL aircraft," *AIAA Scitech 2022 Forum*, American Institute of Aeronautics and Astronautics, Reston, Virginia, 2022.

[8] Raymer, D. P., "Aircraft Design: A Conceptual Approach," , 1992.

[9] Alba-Maestre, J., Beyne, E., Buszek, M., Cuadrat-Grzybowski, M., Montoya Santamaria, A., Poliakov, N., Prud'homme van Reine, K., Salvador Lopez, N., Schoser, J., and Wadia, K., "Midterm Report - Multi-Disciplinary Design and Optimisation of a Long-Range eVTOL Aircraft," Tech. rep., Delft University of Technology, 2021. https://doi.org/10.5281/zenodo.5576027.

[10] Boling, J., and Zha, G. C., "Numerical investigation of longitudinal static stability of a high-speed tandem-wing vtol vehicle using coflow jet airfoil," *AIAA Scitech 2021 Forum*, American Institute of Aeronautics and Astronautics Inc, AIAA, 2021, pp. 1–22. https://doi.org/10.2514/6.2021-1732.

[11] J.A. Mulder, W.H.J.J van Staveren, J.C. van der Vaart, E. de Weerdt, C.C. de Visser, A.C. in 't Veld & E. Mooij, *AE3202 Flight Dynamics Lecture Notes*, Delft University of Technology, Delft, The Netherlands, 2013.

[12] Chen, H., "Effectiveness of Thrust Vectoring Control for Longitudinal Trim of a Blended Wing Body Aircraft," Tech. rep., 2015. URL http://resolver.tudelft.nl/uuid:de4a4261-0948-45e9-9525-b78e2a664af2.

[13] Sadraey, M., *Aircraft Design: A Systems Engineering Approach*, 2012.

[14] Caughey, D. A., *Introduction to Aircraft Stability and Control Course Notes for AE5070*, 2011.

[15] D., S., "Aircraft Design," Tech. rep., Hamburg Open Online University (HOOU), 2017.

[16] O., A.-S., R., A., and H. S., H., "An Educational Rudder Sizing Algorithm for Utilization in Aircraft Design Software," Tech. Rep. 10, 2018. URL http://www.ripublication.com.

[17] O., A.-S., R., A., and H. S., H., "An instructive algorithm for aircraft elevator sizing to be used in preliminary aircraft design software," Vol. 4, 2017, pp. 489–494. https://doi.org/10.5937/jaes15-14829.

[18] Al-Shamma, O., Ali, R., and Hasan, H. S., "Programmable Aileron Sizing Algorithm for use in Preliminary Aircraft Design Software," *Journal of Engineering and Applied Sciences 13*, 2018. URL http://docsdrive.com/pdfs/medwelljournals/jeasci/2018/3458-3462.pdf.

[19] Oliviero, F., "Aircraft aerodynamic analysis – Mobile surfaces on the wing," 2019.

[20] S., G., "Miscellaneous Design Notes," *General Aviation Aircraft Design*, Elsevier, 2014, pp. 947–983. https://doi.org/10.1016/b978-0-12-397308-5.00023-4.

[21] How, J. P., "Aircraft Lateral Autopilots," Tech. rep., Massachusetts Institute of Technology, 2004. URL https://ocw.mit.edu/courses/aeronautics-and-astronautics/16-333-aircraft-stability-and-control-fall-2004/lecture-notes/lecture_12.pdf.

[22] Du, G. X., Quan, Q., Yang, B., and Cai, K. Y., "Controllability analysis for multirotor helicopter rotor degradation and failure," *Journal of Guidance, Control, and Dynamics*, Vol. 38, No. 5, 2015, pp. 978–984. https://doi.org/10.2514/1.G000731, URL https://arc-aiaa-org.tudelft.idm.oclc.org/doi/abs/10.2514/1.G000731.

[23] Du, G.-X., and Quan, Q., "A Matlab Toolbox for Calculating an Available Control Authority Index of Multicopters," , 3 2016. URL http://rfly.buaa.edu.cn/resources.

A. Verification Procedures

A. Verification of Stability Derivatives Model

The verification of the analytical model is performed in a series of steps. First, a number of small unit tests are done in order to verify that the expected change in the stability derivatives is correct. Finally, the model's outputs are compared to already existing aircraft, in terms of magnitude and sign, where the latter is of utmost importance and should be similar for a specific number of stability and control derivatives.

1. Unit test - CG shift

The unit test performed in this subsection is a shift in the CG of the aircraft. In order to perform a complete and concise unit test verification, only a small number of stability derivatives for both longitudinal (C_{X_α}, C_{m_α} and C_{m_q}) and lateral (C_{n_β} and $C_{n_{\delta_r}}$) motions are shown due to their high number.

Specific simplified equations of the change of longitudinal stability derivatives can be found in [11] and are compared to the ones obtained by the code. For the lateral stability derivatives, the qualitative shift is verified. The results of the latter can be summarised in Table 7.

From Table 7, it can be seen that the unit tests are successful. Even though minor differences in C_{m_α} and large differences in C_{m_q} can be seen, these can be simply explained by the fact that the equations used from [11] are simplified and assume a conventional aircraft configuration, which does not have the same analytical equations. Even with these differences, the trend is still the same and hence with the aforementioned the analytical modules have been independently verified.

Table 7 Summarised Results of the CG Unit Test, the expected outcome of those tests and the actual result.

Verification Test	Expected Outcome	Obtained output
Shift in x_{cg} by factor of 2	$\Delta C_{X_\alpha} = 0$ (no dependency) $\Delta C_{m_\alpha} = 11.973$ (destabilising) $\Delta C_{m_q} = -41.1467$ Decrease in C_{n_β} Decrease in magnitude of $C_{n_{\delta_r}}$	$\Delta C_{X_{\alpha_{model}}} = 0$ $\Delta C_{m_{\alpha_{model}}} = 11.756$ $\Delta C_{m_{q_{model}}} = -33.21419$ $\Delta C_{n_{\beta_{model}}} = -0.062499$ $\Delta C_{n_{\delta_{r_{model}}}} = -0.35528$
Shift in x_{cg} by factor of 0.5	$\Delta C_{X_\alpha} = 0$ (no dependency) $\Delta C_{m_\alpha} = -5.986615$ (stabilising) $\Delta C_{m_q} = -5.54833$ Increase in C_{n_β} Increase in magnitude of $C_{n_{\delta_r}}$	$\Delta C_{X_{\alpha_{model}}} = 0$ $\Delta C_{m_{\alpha_{model}}} = -5.878075$ $\Delta C_{m_{q_{model}}} = -12.9931$ $\Delta C_{n_{\beta_{model}}} = 0.028641$ $\Delta C_{n_{\delta_{r_{model}}}} = 0.162813$

2. Comparison with existing aircraft

This subsection briefly presents the strategy to verify the order of magnitude and sign of the stability derivatives using the reference values for different aircraft in clean cruise configuration found in the appendices of [11]. These values are generated using the vortex lattice method.

First, it is essential to mention the differences. The main difference that is observed is the magnitude of the derivatives: $C_{m_q}, C_{Z_{\dot\alpha}}, C_{m_{\dot\alpha}}, C_{m_{\delta_e}}, C_{Z_{\delta_e}}$ and for certain aircraft the down-force $\hat{u}$-derivative C_{Z_u}. For C_{m_q} and $C_{Z_{\delta_e}}$, it can be explained by the fact that both wings are far from the centre of gravity and hence acting as a canard and a tail simultaneously. C_{m_q} is hence approximately doubled, whereas $C_{Z_{\delta_e}}$ is zero due to the way the elevator is used. In fact, the elevator is used in the same manner as an aileron and hence explains that both down-forces for both wings cancel out. This further explains the fact that $C_{m_{\delta_e}}$ is approximately twice as large, as both elevators (instead of one for conventional aircraft) allow for a higher pitching down moment. The $\dot\alpha$-derivatives of the Wigeon are mostly 1.5 to twice as large as reference values, which can be explained by their high sensitivity to the specific configuration and atmospheric conditions. Lastly, C_{Z_u} is significantly smaller than for certain aircraft. This is mainly due to the fact that the eVTOL is flying at subsonic speeds which relates to very low compressibility effects. Additionally, aero-elastic effects which also affect the derivative are neglected.

In terms of similarities, it can be observed that the rest of derivatives have identical sign, especially for the dominant stability derivatives w.r.t to their respective angle rates (q, p and r) and the control derivatives which shows that the model uses the same conventions. Last but not least, the assumption of the derivatives $C_{X_{\dot\alpha}}, C_{X_q}, C_{X_{\delta_e}}$ and $C_{Y_{\delta_a}}$ being zero is also the case of a wide range of different and hence verifying the validity of the assumption.

With the latter, it can be concluded that the model shows results that are very similar to other aircraft and its discrepancies can be easily explained by the dual-wing nature of eVTOL. Hence this confirms that the model can be used as an early preliminary tool to obtain stability and control derivatives of tandem wing (or large canard) aircraft. Computational methods however must still be applied in order to obtain more accurate estimates of the stability behaviour of the aircraft.

B. Verification of Cruise Dynamics Using Numerical Model

In this section the system test to verify the dynamic model is presented. The verification procedure consists of verifying the value of the eigenvalues of the stability matrix **A**. These define the stability behaviour of the different eigenmotions of the aircraft. Before starting the procedure it is essential to mention that the verification model outputs the eigenvalues in normalised form, defined as $\lambda_c = \frac{\bar{c}}{V_0} \cdot \lambda$ for longitudinal motions and $\lambda_b = \frac{b}{V_0} \cdot \lambda$ for lateral and hence must be transformed to their non-normalised form. The results are summarised in Table 8. From Table 8, it can be seen that there is no difference between both models in terms of stability behaviour of the aircraft. The system test is hence successful and the model implementation of the state-space matrices is confirmed to be correct.

Table 8 Eigenvalues computed by the model λ, the numerical model for verification normalised λ_c or λ_b eigenvalues and the error

Eigenmotion	**Model eigenvalue** λ	**Numerical model eigenvalue** $\lambda_{\mathbf{c}}$ or $\lambda_{\mathbf{b}}$	**Error:Re**(λ), **Im**(λ) **(%)**
Short period	$-2.47; -0.89$	$-0.04332; -0.01557$	0, 0
Phugoid	$-0.0226 \pm 0.0361j$	$-0.0003960 \pm 0.0006318j$	0, 0
Aperiodic roll	$-2.52 \pm 0j$	$-0.28690 \pm 0j$	0, 0
Dutch roll	$-0.00699 \pm 0.97j$	$-0.0007948 \pm 0.1103j$	0, 0
Spiral	$0.0125 \pm 0j$	$0.0014239 \pm 0j$	0, 0